Dosimetry for MARS

A THESIS SUBMITTED TO

THE PHYSICS AND ASTRONOMY

OF UNIVERSITY OF CANTERBURY

IN FULFILMENT OF THE REQUIREMENTS FOR THE DEGREE OF

MASTER OF SCIENCE

Gray Siyuan Lu

Physics and Astronomy

University of Canterbury

March 2016

Abstract

MARS spectral CT is an up and coming imaging modality which shows great promise in revealing unique diagnostic information and industrial analysis techniques. Because this imaging modality based on X-ray CT, it is of utmost importance to study the radiation dose aspects of its use. Moreover, the capabilities of spectral imaging show potential for a new method in 3D dosimetry, one which is personalized.

This thesis reports on the use of Monte Carlo simulation tool TOPAS in estimating the dose to a sample scanned with the pre-clinical MARS scanner, and the results are experimentally verified using an ion chamber and TLDs. Use of EPDs in characterizing radiation within the gantry was also investigated. In addition, a pilot study was conducted into a potential algorithm a future on-board personalized dosimetry system may utilize. On the whole, all dosimetry techniques indicate a MARS scan dose on the order of 20 mGy.

Acknowledgments

Firstly thanks to my supervisors Dr. Steven Marsh and A/Prof. Anthony Butler for their moral support and gentle guidance. Meetings at the commencement of my research imbued a balance of optimism and pragmatism to begin this journey.

Many thanks Pierre Carbonez and Jerome Damet for their support from the other side of the world. Their 3 monthly visits kept me on track and provided me with a healthy amount of constructive criticism and suggestions. Thanks to Dr. John Laban, Dr. Sophie Walker, and Dr. Nick Cook for their expertise and access to dosimetry equipment as well as helpful consultation.

Special thanks to Dr. Christopher Bateman for day-to-day student supervision, and Prof. Philip Butler for his authoritative management.

Thanks to the MARS team, especially Dr. Stephen Bell, Dr. Michael Walsh, and Dr. Raja Panta for technical support around the MARS scanner hardware and software. Also, thanks to Robert Thirkettle for his help in phantom design and fabrication.

Finally thanks to fellow students Marzieh Anjomrouz and Muhammad Shamshad for the opportunity to share knowledge, tools, and occasionally data. Also, thanks to Srinidhi Bheesette for being a good 'lab partner'.

Academic contributions

During the course of this thesis I have contributed to the MARS project through implementations of dosimetry procedures and development of a Monte Carlo tool, paving the way for future development of an on-board personalized dosimetry system. I have also made the following contributions:

- Oral presentation of 'Dosimetry for MARS' at *Centre for Bioengineering Mini-Conference*, 29th July 2015. This is a conference held in Christchurch held 3 times a year, and allows local researchers to open their work up to an audience of peers.

- Oral presentation of 'Dosimetry for MARS' at the *University of Canterbury 32nd Annual Physics Department Conference*, 22nd September 2015. This conference allows student research to be shared with the staff and other students of the rest of the department.

- Contributed to bug reporting and feature improvement to the TOPAS software development. This feedback has been incorporated into TOPAS and distributed to researchers around the world.

- I was awarded a summer research scholarship to study spectral quantification of bone mineral density, which helped initiate collaboration between MARS and Oregon State University. This collaboration with a well funded organization has opened new doors for collaborative research, and expands of the influence of MARS spectral imaging internationally.

- Provided consultancy on Monte Carlo and dosimetry issues to PhD students and fellow MARS team members Marzieh Anjomrouz and Muhammad Shamshad. Sharing of data has been mutually beneficial in adding depth to each students' work.

- Co-authored a manual to the spectral imaging visualization software MARS Vision with Srinidhi Bheesette. The manual became the standard reference for all users of MARS imaging.

- Provided introductory orientation in MARS imaging and project consultation to new PhD students Srinidhi Bheesette and Chikezie Onyema. This accelerated the students' integration into MARS team and helped clarify their potential research directions.

- Aided in maintaining collaboration between MARS, NCRS/ESR and CERN dosimetry service. The work in this thesis was among the shared research interests between the different groups, who form a network of specialized facilities and expertise.

Nomenclature

Abbreviations

ALARA	As low as reasonably achievable
CAD	Computer aided design
CERN	European Organization for Nuclear Research
CMOS	Complementary metal oxide semiconductor
CT	Computed tomography
CTDI	Computed tomography dose index
DICOM	Digital Imaging and Communications in Medicine
DNA	Deoxyribonucleic acid
DRL	Diagnostic reference level
EPD	Electronic personal dosimeter
GEANT	Geometry and tracking
HU	Hounsfield unit
HVL	Half value layer
Kerma	Kinetic energy released per unit mass

MARS	Medipix All Resolution Systems
MD	Material decomposition
MOSFET	Metal oxide semiconductor field effect transistor
NCRS	National Centre for Radiation Science
ODD	Object detector distance
PMMA	Polymethyl methacrylate
PTB	Physikalisch Technische Bundesanstalt
SI	International System of Units
SOD	Source object distance
TLD	Thermoluminescent dosimeter
TOPAS	Tool for particle simulation

Terminology

Absorbed dose	Radiation energy absorbed per unit mass
Air kerma	Kerma in air
Cavity theory	Theory relating air kerma to absorbed dose
Gray	SI unit for absorbed dose
Overarching project	Past, present, and future dosimetry work for MARS
Sievert	SI unit for equivalent/effective dose
W-value	Average energy required to produce ion pair

Table of Contents

Chapter 1

Introduction

1.1 Overview

Spectral X-ray imaging has been heralded as the next big step in medical imaging, offering the capability to use X-ray 'colours' to distinguish materials within scanned objects. This technology promises to supersede greyscale computed tomography (CT) from which it was based, and it also shows potential to open up new areas of analysis and diagnosis that threaten a myriad of existing modalities [Anderson and Butler, 2014]. The ultimate goal of the Medipix All Resolution Systems (MARS) group is the establishment of a local industry revolving around the development and manufacture of this innovative new spectral X-ray imaging modality - dubbed the MARS scanner.

However it is crucial one does not forget that for all medical tools based on ionizing radiation, radiation dose must be a key consideration from early development through to clinical use. A simple look at history warns of the serious health consequences of a lax attitude towards radiation dose in imaging [Smith-Bindman, 2010][Colang et al., 2007][Brenner and Hall, 2007]. The existence of organisations dedicated to reducing unnecessary diagnostic radiation exposure [Goske et al., 2008] further highlights the gravity of this issue.

The MARS group is fast approaching the transition from spectral scanning of small animals to full size human scanning. In response to this, questions more often being asked by the community are: How much dose does it give? What is the minimum dose it needs to achieve its purpose? How does the dose compare to existing CT systems? Given the differences in the underlying processes and in the applications of the MARS system, it is possible the latter question may not

be appropriate. A MARS scan yields considerably different information, and so the MARS scanner may have different exposure requirements from conventional CT scanners. It is likely that simple reliance on the same conventions - the protocols and policies of appropriate use - followed by other CT systems will not be sufficient.

Guidelines in how a MARS scanner should be used to achieve each of its diagnostic goals while minimizing dose will eventually need to be established. At this relatively early stage in development we can begin laying the groundwork for a full consideration of dosimetry in anticipation of the future human MARS scanner. Given the capabilities of spectral detection, there is even potential for the development of new dosimetry techniques and perhaps even the advancement of the field of dosimetry.

The work in this thesis focuses on developing tools and methods for quantifying radiation dose in a MARS scan. Primarily, modeling is done with the Monte Carlo simulation codes GEANT4 [Agostinelli et al., 0038] and TOPAS [Perl et al., 2012]. This model aims to simulate all fundamental scanner parameters and predict spatial dose distribution - thus evaluating absorbed dose to specific organs - for any scanning protocol. Part of the work involves verification of simulation results with physical measurement. The resultant tool would then become an essential provider of comparison data for future radiation and dosimetry studies, able to be scaled up for a human MARS scanner.

Fundamentally, knowledge is needed on how best to use MARS spectral imaging technology so it will be both effective and safe for routine clinical use. This seemingly simple idea is in fact intimately influenced by multiple fronts: by the developers, constantly improving the hardware and software of the imaging chain on the quest for better data; by the applications research, investigating ways to apply the technology and exploring diagnostic requirements of image quality. While these areas of progress are concerned with attaining development of an effective scanner, advocacy is needed for the safety aspect.

1.2 Significance

Through collaboration with CERN Dosimetry Service, National Center for Radiation Science (NCRS), and Christchurch Hospital, the overarching project encompassing this present study strives to ensure the issues of radiation and dose are

at the forefront of scanner development. The first study in the overarching project was conducted by Noemie Ganet [Ganet, 2014], who began by investigating methods of measuring the radiation dose to simple phantoms in the MARS small animal scanner. To expand on this work, the present study aims to use Monte Carlo simulation as a tool for estimating the 3D spatial dose deposition in any scanned sample - accurately showing dose in places where physical measurement is not feasible.

In the future, the overarching project strives for an advanced dose monitoring functionality within the spectral imaging system. Such a system could infer directly from scan data exhaustive information on patient dose and aid in dose optimisation for new applications.

1.3 Thesis outline

The remaining portion of this chapter will highlight fundamental concepts necessary in understanding the subject matter of this thesis.

A major part of this thesis focused on implementing a flexible Monte Carlo simulation of radiation dose in the pre-clinical MARS scanner. This is covered in chapter 3, which introduces the concepts of Monte Carlo simulation and begins by briefly discussing the GEANT4 and TOPAS codes. Further on, chapter 3 covers the procedures followed in crafting a TOPAS simulation capable of scoring spatial dose distributions in complex objects. Also in this chapter, non-Monte Carlo methods of calculating dose are explored and compared alongside Monte Carlo results; the last of these also serves as a feasibility study into how a future on-board dosimetry system may operate.

Chapter 4 covers the process of experimentally verifying the Monte Carlo simulation capability using ionization chamber equipment and TLD within the MARS scanner. In addition, a preliminary study in the use of EPD within the scanner was conducted and covered in this chapter.

Much of the experimental methodology and sources of expertise employed in chapter 4 were previously established in the pilot study conducted by Noemie Ganet. Key aspects of her work directly lead to significant portions of the work in this thesis and are described in chapter 2. Alongside this, the core concepts behind each dosimeter device are briefly explained.

The thesis will conclude with Chapter 5, discussing the impact of the present

work and outlining the next steps in the overarching project.

1.4 Prerequisite knowledge

Comprehension of the current work requires a minimum prerequisite understanding of particular areas of science. This section aims to highlight the importance these fundamental concepts have in the context of this thesis. As they are generally well understood topics, it will be left up to the reader to seek external sources for more thorough descriptions in areas of interest.

X-rays for medical imaging

X-rays are a type of electromagnetic radiation with a shorter wavelength than visible light. X-rays in imaging are typically generated by X-ray tubes, mainly through the bremsstrahlung effect and characteristic emissions. The MARS scanner features such an X-ray source, and this is the cause of radiation dose. Hence characterising the output from an X-ray tube is a prominent part of this work. Readers requiring further information on the well-known topic of X-ray generation can refer to any reputed imaging physics textbook such as Hendee and Ritenour [2002].

Fundamental X-ray interactions

When X-rays travel through an object, some of the photons may interact with the obstructing matter; in fact the partial obtrusion of X-rays is what makes radiological imaging possible. Photons can interact with the atoms and molecules of matter in a plethora of ways, each individual type of interaction combining to form the overall attenuation. Energy from the incident beam may be taken up by atoms or molecules to form higher energy states, or dislodge electrons to form charged particles. The aftermath of such events could include re-emission of photons or electrons of the same or different energies to the primary radiation particle. While each interaction type is stochastic, their relative chances of occurring change with the energy of the incident radiation beam; similarly the overall effect of attenuation is dependent on the material composition of the attenuating object.

It is only with an understanding of the principle interactions between X-rays and matter that one can truly appreciate the mechanisms underlying formation of images, and how radiation ultimately affects living tissue. As with basic X-ray generation, interested readers may find more details regarding particle interactions and imaging physics in textbooks such as [Podgorsak, 2005] , [Hendee and Ritenour, 2002], [Dance et al., 2014], [Bushberg et al., 2012].

Radiation dose

Radiation dose refers to the deposition of energy in matter due to radiation. The physical quantity of absorbed dose is measured as energy deposited per mass in joules per kilograms, or the unit Gray. At the biological level, radiation and the charged particles formed by it can harm cells through damage to DNA. Manifestations of biological damage may take the form of deterministic effects such as necrosis, whose severity rises with increasing dose. They may take the form of stochastic effects such as cancer, for which incidence rises with increasing dose. It is generally assumed that there is no dose below which one is safe from stochastic effects; this is the basis of the 'As Low As Reasonably Achievable' principle (ALARA) within radiation protection [ICRP103, 2007], as a general policy to keep adverse effects to a bare minimum.

Though ionizing radiation provides the means of producing informative images, it is a potential source of harm to humans and animals. MARS spectral imaging is no exception, and one of the motivations behind this project revolves around the idea that radiation dose in spectral imaging need to be quantifiable with the highest possible precision.

Further information regarding radiation protection and radiobiology can be found in reputed medical physics textbooks and publications by international bodies [Hall and Giaccia, 2012] [ICRP103, 2007].

Radiation dose quantities

Absorbed dose in the SI units of Gray is the physical measure of radiation dose. Because the primary concern is on biological effects of radiation however, other measurement units known as protection quantities have arisen. Equivalent dose is one such concept which accounts for biological effects to an organism by considering the relative effect of different types of radiation particles; effective

dose in addition considers the relative importance of each affected organ. These quantities are given in units of Sieverts (Sv), but in practice is not directly measurable.

The convention of operational quantities were made to address the practical limitations of measuring effective dose. These quantities were designed to be a measurable but conservative estimate of protection quantities, and are based on point doses determined at defined locations in defined phantoms. Included are the ambient dose equivalent $H_*(d)$, directional dose equivalent $H'(d,\Omega)$, and personal dose equivalent $H_p(d)$ - the bracketed variables specifying depth and angle within the specified phantom.

Another quantity measured by many dosimeters is the kerma, also an acronym for Kinetic Energy Released per unit MAss. This quantity is similar to absorbed dose, also measured in units of Gray but specifically refers to the energy of the liberated charged particles. Energy transferred to electrons by photons can be dissipated in two ways: through collisional interactions like ionization or excitation, or through radiative processes like bremsstrahlung. Hence total kerma is said to be made up of collisional kerma K_{col} and radiative kerma K_{rad}. Under specific conditions, collisional kerma equates to absorbed dose.

Different instruments are made and calibrated to measure different quantities. Because the various quantification methods used in this study are not necessarily equivalent, it is crucial to that how each quantity relates to the others be kept in mind. More exhaustive definitions of radiation dose quantities can be found in radiation physics textbooks and publications by international bodies [Mattsson and Soderberg, 2013][ICRP74, 1996].

Medipix detectors and spectral imaging

The MARS scanner, which this overarching project is based around, is the result of applying the spectroscopic X-ray detector Medipix3RX to biomedical imaging. Medipix3RX, developed at CERN (European Organization for Nuclear Research), is composed of a semiconductor sensor layer connected to a CMOS (complimentary metal oxide semiconductor) pixel detector readout chip. The feature of Medipix3RX detectors is the ability to tell apart incident photons by energy.

The X-ray attenuation properties of a material are a function of photon energy, thus the ability to differentiate photons by energy allows identification of specific

materials. With Medipix3RX, materials previously indistinguishable due to having similar densities can now be identified based on different spectral attenuation profiles in a process known as material decomposition (MD).

Figure 1.1: *Photograph of the MARS scanner exterior and the interior with the covers open. The spatial axes of the gantry are indicated.*

The MARS team have implemented spectral CT at a pre-clinical stage, currently basing development on small bore scanners as shown in figure 1.1. Such a technology promises improvements in capability over conventional CT systems and other imaging modalities through improvement in image quality, reduction of beam hardening artefacts, superior detection and hence use of contrast agents, and improved tissue contrast.

Hand in hand with greater capabilities is enhancement in diagnostic potential for a variety of diseases, and hence better clinical outcomes. One example of a rising application is the spectral molecular imaging of atherosclerosis, the basis for cardiovascular disease and stroke. Spectral scanning shows promise in the ability to detect and monitor vulnerable plaque by imaging the composition of plaque and determining its likelihood of rupture. Studies have already been conducted on excised human carotid samples. Another rising application is in cancer imaging, specifically the simultaneous imaging of multiple biomarkers and of high-Z nanoparticles bound to cancer seeking drugs, biomarkers or antibodies. Detecting abnormal changes in biomarkers may be the key to early detection of physiological changes signaling cancer at a curable stage. Meanwhile, superior specificity in monitoring high-Z particles promises to reveal molecular response of cancer to drugs. Studies in these applications have already been conducted on mice.

Interested readers seeking specific information on detector mechanisms and

spectral imaging may refer to publications on spectral detectors and MARS [Anderson and Butler, 2014][Yu et al., 2012] [Cambell et al., 2016] .

Chapter 2

Vanguard MARS dosimetry studies

2.1 Overview

Lesser dosimetry studies for the MARS imaging system have been done in the past, most recently by Noemie Ganet [2014]. Ganet's work focused on initial development and implementation of a dose measurement procedure for the MARS small bore scanner. These procedures provided a guideline in methodology for subsequent dosimetry work such as the practical portion of this thesis, which is covered in chapter 4. While the work in this thesis has greatly improved and expanded on the methodology developed by Ganet, core aspects of the experimental procedures were retained. Also, many of the decisions made in the present work directly address limitations revealed by Ganet. For this reason it is pertinent to review the work conducted by Ganet in this chapter.

During Ganet's study, collaboration with NCRS, CERN dosimetry service, and Christchurch Hospital provided radiation dosimetry expertise and support. Collaborating groups contributed through the provision of facilities for TLD calibration and readout, expertise in TLD and ion chamber dosimetry and access to equipment. These collaborating partners were again called upon during work in this thesis, in order to continue the overarching project.

The methodology and preliminary results of Ganet's study using an ion chamber and TLDs are reviewed in this chapter. Alongside this, principles of ion chamber and TLD operation will also be reviewed.

2.2 Ionization chamber

Ion chambers are among the most mature and widely used types of radiation dosimeters. Their use is especially prominent in the assessment of dose for CT scanners, thus prompting Ganet to include ion chamber dosimetry in her work.

This section will first briefly explain the concepts behind the operation of these devices: the basic design, the mechanisms of acquiring signals, and the definition of the commonly used computed tomography dose index (CTDI). Following this, the procedure of Ganet's ion chamber study will be reviewed.

2.2.1 Principles of ion chamber dosimetry and CTDI

When a fast charged particle such as electrons released by X-ray interaction with materials travels through a gas, it may interact with a gas molecule. In this interaction, if the energy transferred by the particle to the gas molecule exceeds the ionization energy (the W-value, in practice) of the molecule, an ion pair may be formed. If it is possible to measure the amount of ion pairs formed, then it is possible to determine the amount energy deposited by the radiation and hence the radiation dose - this is the essence of how an ion chamber works.

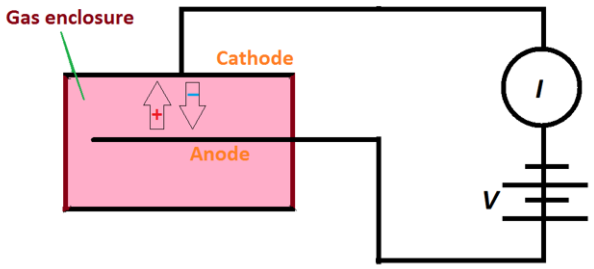

Figure 2.1: *Basic circuit diagram of an ion chamber. Ionizing radiation causes the formation of ion pairs within the gas chamber, which move according to the electric potential and form a measurable current.*

To enable measurement of ion pair formation, an external electric field needs to be applied to the region to cause the ions and electrons to move away from their point of origin. This constitutes an electric current which can be measured; a diagram of such a setup is shown in figure 2.1. Assuming recombination is

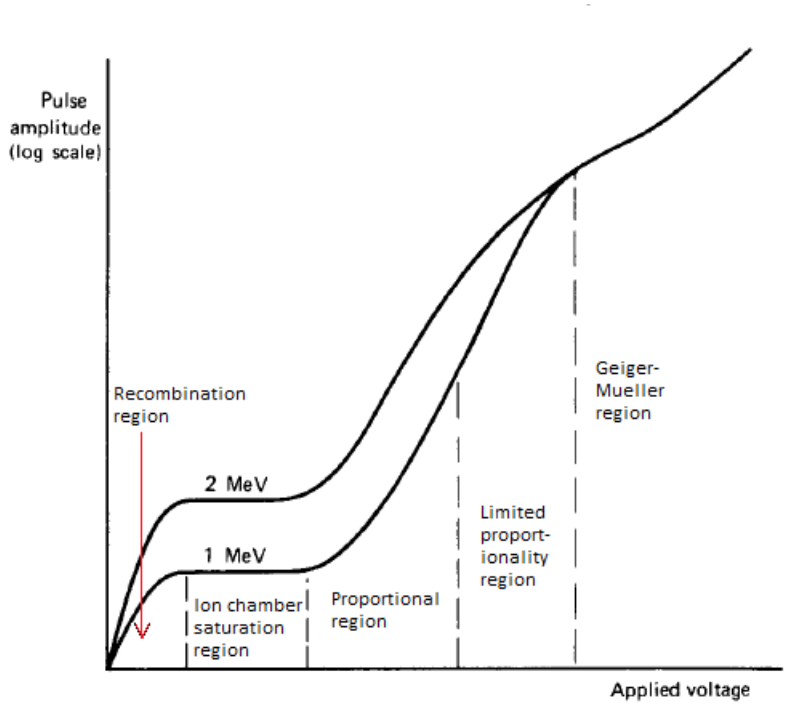

Figure 2.2: *The current voltage characteristics of a gaseous radiation detector for two grades of radiation exposure[Knoll, 2000].*

negligible and all charges are efficiently collected, the current produced is a measure of the rate at which ion pairs are created within the gas chamber and hence the rate of radiation dose can be inferred. For this assumption to be correct, the applied voltage must be at a sufficient level to minimize or eliminate recombination of ion pairs.

Figure 2.2 shows how increasing the detector operating voltage can increase the amount of ions collected, or the measured current. We see that as voltage is increased from very low levels up to the ionization chamber region, the amount of current measured can be increased; this reflects the reduction of recombination events ensuring the measured current accurately portrays the number of ion pairs created in the volume. The measured current is an indication of the exposure, and can be related to the dose via cavity theory or calibration. While not relevant for this work, even higher applied voltages are used for slightly different types of radiation measurement - proportional counters and Geiger Muller counters [Knoll, 2000].

Computed tomography dose index

Raw values of measured dose can be processed in different ways. CTDI is a quantity which aims to describe the radiation dose given by a CT scan independent of what is scanned. This quantity is commonly used to grade the dose performance of a particular scanner and scan protocol against a national diagnostic reference level (DRL) for safety purposes.

More specifically, CTDI is a measure of average absorbed dose in the axial direction (or z-axis) while undergoing a CT scan. It is typically measured within a standardized phantom using a pencil ion chamber, from one axial CT scan of a single X-ray source rotation. It is calculated by integrating the absorbed dose and dividing by the nominal beam collimation according to the following equation:

$$CTDI = \frac{1}{NT}\int_{-\infty}^{\infty} D(z)dz \tag{2.1}$$

Where N= number of tomographic slices imaged in single axial scan, T=thickness along the z-axis of a tomographic slices, D(z)=radiation dose profile along the z-axis.

Practically however, the limits of ∞ and -∞ are unrealistic. Using a 100 mm pencil chamber, the measured quantity is $CTDI_{100}$ which is the accumulated scan dose at the center of a 100 mm scan is divided by the nominal beam collimation.

$$CTDI_{100} = \frac{1}{NT}\int_{-50mm}^{50mm} D(z)dz \tag{2.2}$$

For relatively large bodies like that of a human, absorbed dose at the peripheries or edges cannot be expected to be the same as absorbed dose at the core. This is accounted for by a weighted measure, $CTDI_w$, which includes 5 measurements within the phantom: 4 near the edges and 1 at the center. $CTDI_w$ is calculated by the following formula, where the average of the 4 edge measurements is used for the second term:

$$CTDI_w = \frac{1}{3}CTDI_{100,centre} + \frac{2}{3}CTDI_{100,edge} \tag{2.3}$$

Traditionally, the two phantoms commonly used are the 160 mm diameter cylinder representing the head and 320 mm cylinder representing the body [Dance

et al., 2014]. For reference, European multi-detector CT DRL for adults are stated to be 60 mGy for head, 30 mGy for chest, and 35 mGy for abdominal scans [Tsapaki et al., 2006]. These values are in $CTDI_w$.

2.2.2 Ion chamber methodology

The following section describes the methodology established by Ganet in obtaining first estimates of radiation dose in the MARS scanner using an ion chamber. Details of the equipment are also described.

The work done by Ganet contributed to this thesis by providing a guideline in ion chamber usage within the MARS scanner, accompanying phantom and holder equipment, and also demonstrated a basic approach to analysis. In following these procedures, shortcomings were identified; this preceded the formulation of a more complex experimental procedure (see chapter 4).

Equipment

The device used was an Unfors Raysafe Xi CT detector. This has an active length of 100 mm and auto correction for temperature and pressure, measuring between 1 and 9999 mGy and an expanded uncertainty on dose (at reference beam RQA9) below 5%. The dose systems are calibrated by PTB (Physikalisch Technische Bundesanstalt), traceable to NIST (National Institute of Standards and Technology) and PTB. The thin shape allows placement in the various holes on a standard CTDI body or head phantom which would typically lead to calculation of $CTDI_w$. A USB cable connects the pencil detector unit to a readout or electrometer unit which displays measured values in real time.

For the MARS small bore scanner, specimens used are generally too small to utilize a $CTDI_w$ phantom and so a basic 'CTDI' is simply measured at the centre of a 30 mm diameter cylindrical Polymethyl methacrylate (PMMA) phantom. The material was chosen to be cheap and near water-equivalent. A tunnel runs through the central axis of the phantom allowing entry of the pencil chamber with little clearance. The phantom (shown in figure 2.4) and accompanying phantom holder were specifically fabricated for this experiment.

Figure 2.3: *Ion chamber equipment - Unfors Raysafe Xi CT detector.*

Measurement

Initial steps in measurement began by attaching the phantom to the phantom holder, then inserting the pencil detector through the end of the phantom. This setup was then mounted securely to the scanner sample bed. The USB cable was then threaded through gaps in the gantry such that the pencil detector unit could be connected to the readout unit placed outside the gantry. This required removal of some of the outer covers of the scanner, and care had to be taken that the cable was not tangled during gantry rotation. The scan was run such that the source was aligned with the middle of the pencil detector, and only a single gantry rotation without sample translation was involved. The following scan parameters were used:

- X-ray tube voltage was set to 120 kVp
- Tube current was 50 μA
- 90 ms exposure (acquisition) time per frame
- 180 projection frames per rotation
- Source to object distance (SOD) was 140 mm
- Object detector distance (ODD) was 80 mm

These settings were also applied to measurements in the subsequent section with TLDs.

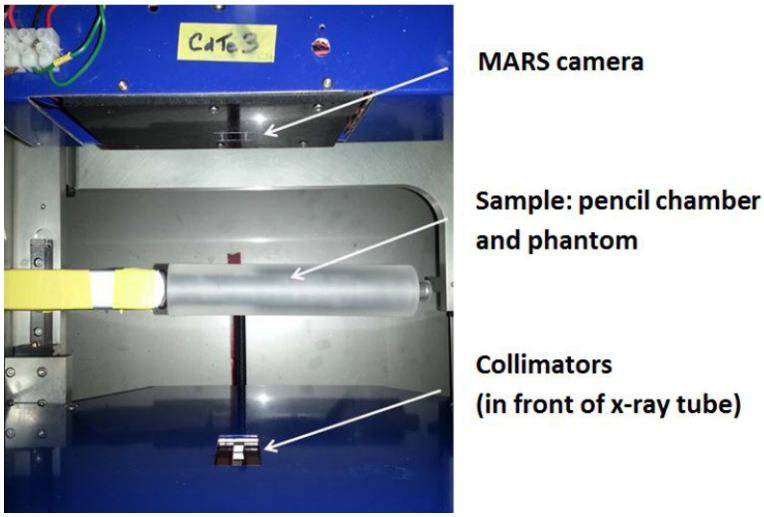

Figure 2.4: *Pencil chamber within PMMA phantom, placed within the gantry of MARS unit 11 [Ganet, 2014].*

Because the measurements are done within a non-standard phantom, the measured value is technically not the CTDI but will still be referred to as such. The quantity of CTDI is essentially the dose per slice, thus to convert the measured dose to CTDI the exposed slice thickness is required. Using Gafchronic film to measure the collimated field size, the exposed length of the phantom was found to be 9 mm along the sample (z) axis for this scan protocol. Similarly the field size at the detector plane was found to be 15x15 mm, which covers the 14x14 mm single detector chip.

Analysis

To convert the measured value to CTDI, the following equation was used:

$$CTDI = \frac{energyIntoSlice}{massOfSlice} = rawMeasurement \times \frac{lengthOfChamber}{sliceWidth} \tag{2.4}$$

As the chamber measures dose to its entire length, what is measured is actually the energy deposited into a slice averaged over a region greater than the slice. This equation scales that value by how much longer the dosimeter is compared to the length that was irradiated, effectively assigning the measured dose in the whole phantom to the one slice.

Measurement was done with two cases of filtration: no added filtration, and 2 mm Al added filtration; CTDI was found to be **28.7±1.4 mGy** without filtration, and **18.3±0.9 mGy** with 2 mm Al.

It was noted that a significant portion of the given dose does not actually come from the stated exposure time; 180 projections of 90 ms exposure time each should result in a scan time of 16 s, but instead the scan took 53 s. For a similar scan with 720 projections, the scan time was found to be 232 s instead of the expected 65 s. This excess exposure is partly due to the time taken for the chip to process frame information and prepare itself for the acquisition of the next frame. This will be henceforth referred to in this thesis as the readout time. MARS development has stated that improvements to the software can gradually reduce this time, and hence improve the dose efficiency of the system.

2.3 Thermoluminscent Dosimeters

Thermoluminescent dosimeters, or TLDs, are another versatile form of dosimeters. The TLD experiments were conducted to both cross check with the ion chamber measurements, and to obtain additional information. As TLDs are much smaller than a pencil ion chamber, it becomes more feasible to measure dose as a function of depth within such a small phantom.

This section will first explain the concepts of how TLDs function, before detailing the core aspects of Ganet's work with TLDs.

2.3.1 Principles of TLD

The essence of thermoluminescent dosimetry is in storing radiation energy within an exposed material, then releasing that energy in the more measurable form of visible light. Materials with such capabilities are inorganic crystals purposely made with particular concentrations of impurities or defects. When exposed to ionizing radiation, electrons can be excited into the conduction band forming a

free electron hole pair (analogous to an ion pair). In pure crystals the pair would likely recombine promptly, emitting light through fluorescence. In thermoluminescent materials the defects act as bandgap trapping centers, reducing the likelihood of prompt recombination at room temperature by providing a metastable state for the electrons and holes. If additional thermal energy is applied to the crystal trapped electrons can be re-excited to the conduction band, enabling them to migrate to holes for recombination. The transition in energy states causes the emission of a thermoluminescent photon, depicted in figure 2.5 [Knoll, 2000].

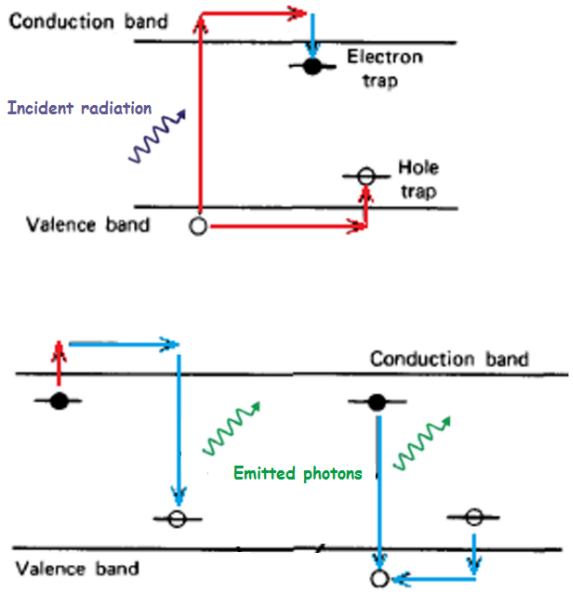

Figure 2.5: *Diagram representing the electron hole energy transitions in a TLD material. Top - formation of electron hole pair with ionizing radiation. Bottom - two possible modes of recombination upon raised temperature, leading to photon emission [Knoll, 2000].*

TLD systems typically utilize photo-multiplier tubes to obtain light yield during heating. The amount of light released can be related back to the number of electron-hole pairs created, and hence the amount of radiation exposure experienced by the material [Bushberg et al., 2012]. It should be noted that the measured signal due to this emission of light is heavily dependent on the exact process of heating. If unaccounted for, a single TLD may give different values for the same exposure on different readout instances; how this is addressed is described later. Once the signal has been read, the sample can then be raised to

an even higher temperature in order to 'erase' all remaining trapped charges. This enables TLD chips to be reused.

2.3.2 TLD methodology

This section describes the methodology developed by Ganet, and tools used in obtaining first estimates of radiation dose in the MARS scanner using TLD.

As TLDs were also used for practical work in this thesis, the same calibration and handling procedures followed during Ganet's TLD experiment were again applicable. Like with the ion chamber experiment, phantoms designed and fabricated by Ganet for TLD measurements were inherited for use in experiments in this thesis. Furthermore, results obtained by Ganet shed greater light on an issue relevant to the dose performance of the MARS scanner; this issue was addressed for the experiment conducted in this thesis (see chapter 4).

Equipment

TLDs used in this experiment had shapes of small disks 4.5 mm diameter and 0.8 mm thickness, produced by China National Scientific Instruments and Material Corporation. Marked GR-200A, these TLD 'chips' consist of Lithium Fluoride (LiF) crystals doped with Cu, Mg, and P. A Harshaw model 5500 automatic TLD Reader was used to extract measurements of dose from the TLDs. For this experiment, one full carousel of 50 TLD chips was used.

Because of the difference in dosimeter used, a separate phantom was required to make measurements with TLD. The phantom was again based on a PMMA cylinder 30 mm in diameter and used the same phantom holder as the ion chamber phantom. Various cylindrical holes were drilled at various depths to allow placement of the TLD chips, and PMMA rods were inserted into these holes to keep the chips in place and maintain the scattering conditions of a solid phantom. However because TLD are known to be directionally sensitive [Dieterich et al., 2016], a second TLD phantom was made in which the cylindrical holes were drilled along the long axis of the phantom. This way, when the phantom is inserted into the MARS scanner, rotation of the gantry will not change the orientation of exposure for the TLDs, as they are rotationally symmetrical in that plane. The drawback of this phantom is there is less space to drill holes and so fewer depths can be sampled. The two phantoms were designated *phantom S* for the directionally

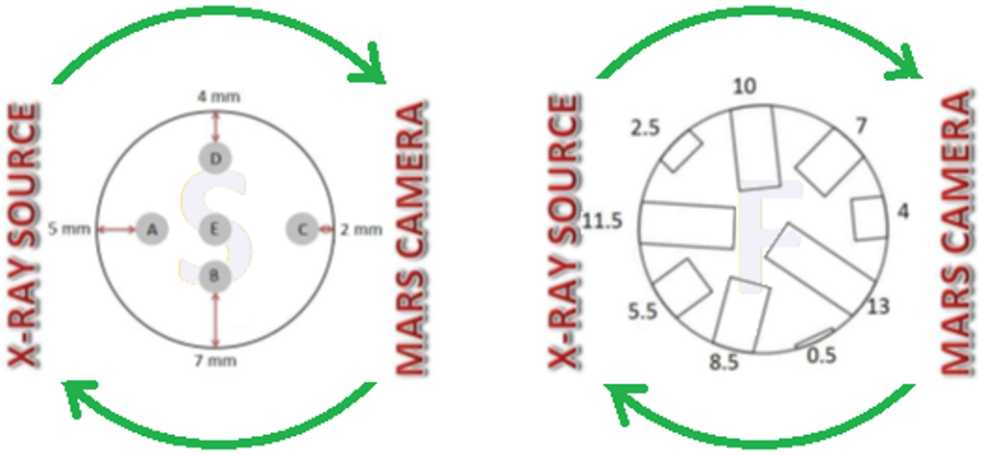

Figure 2.6: *Transverse cross sections of each phantom used for TLD measurements, shown in relation to the direction of source and camera at starting position. Left - phantom S; Right - phantom F [Ganet, 2014].*

independent one and *phantom F* for one allowing some face-on irradiation (figure 2.6).

Equipment related to calibration included a Pantak HF320/420 X-ray generator connected to a Comet MXR-321 X-ray tube; this source allowed for variable tube potential and filtration. An NCRS medium energy free air transmission monitor chamber operated as a primary standard provided the basis for calibration.

Calibration process

Reading out exposed TLDs produces raw values in units of charge. To relate this to air kerma experienced by the exposed TLD chip, a number of factors must be taken into account:

I Basic calibration, how much charge corresponds to a given amount of air kerma exposure on a typical TLD chip.

II Small variations between the luminescence of each individual TLD for the same exposure. This is likely due to subtle differences in the microstructure of each TLD chip as they are not always fabricated perfectly identically.

III Energy structure of the beam

IV Slight variation in readout process taking place between readout of calibration exposures and each readout of measurement exposures.

V Direction of exposure

VI Background radiation / noise

These factors were taken into account via the following corrections:

1. **Energy calibration:** A set of 8 TLD were exposed to an X-ray beam of 120 kVp and 4.28 mm Al half value layer (HVL) - chosen to closely match the beam quality for the selected MARS scan protocol. The TLD were suspended in free air using plastic wrap, irradiated with a 15 cm beam field 100 cm from the source (figure 2.7). The amount of air kerma applied was measured by monitoring the irradiation time and measuring the air kerma rate via the transmission monitor chamber. The mean readout value in Coulombs relative to this kerma gives a correction coefficient which accounts for both factors I. and III. from the previous list.

2. **Individual response:** Each of the 50 TLD were exposed to 50 mGy of air kerma from a Co-60 source and the readout response from each TLD chip is compared to the average of all chips to obtain a set of individual correction coefficients. This accounts for factor II. from the previous list.

3. **Readout process:** A set of 5 TLD were always set aside only to be irradiated under the same conditions as described in correction 1 each time the carousel of TLD chips are read out. Changes in the mean of these 5 chips between different readouts gives a correction coefficient for any potential differences in readout process itself between different instances, and corrects for factor IV. from the previous list.

4. **Background subtraction:** A single TLD is not irradiated after annealing. The raw value obtained from reading this blank chip is subtracted from all others.

Alongside Ganet's main experiment, TLD angular response was tested. They were observed giving around 6% higher signal when irradiated on the flat face compared to their side face. One way to rationalize this is consideration of

Figure 2.7: *Photograph of 8 TLD chips suspended by cling film, in preparation for controlled irradiation for calibration purposes.*

the energy structure of the beam: low energy photons tend to be stopped more easily and hence deposit their energy at a shallower depth, whereas higher energy photons tend to be more penetrating. When exposed on the broad side, TLD chips experience a greater cross sectional area of the photon beam and the amount of low energy photons depositing their energy is greater. When exposed on the narrow side, there is a smaller cross sectional area but a greater depth for the photons to penetrate; higher energy photons have a greater opportunity to eventually deposit their energy, but this does not offset the relative absence of low energy photons. This is an issue because chips are calibrated at a particular orientation, thus readout values assume measured irradiation was also at the same orientation. This can be problematic as the orientation of TLDs relative to the beam may change with CT gantry rotation. For Ganet's study, all TLD chips were calibrated face-on.

Measurement

Each phantom was loaded with one TLD per slot and mounted onto the sample bed as shown in figure 2.8. The scan was set to the same parameters as described in section 2.2.2, where the source and camera position was centered on the position of the TLD chips. Following the scanning session, the TLD chips were returned to the carousel and taken to the reader. The read-out pro-

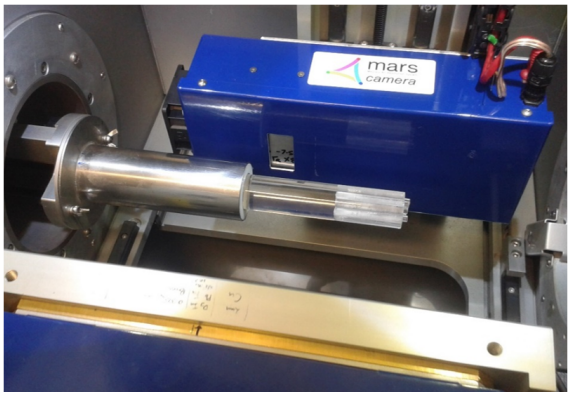

Figure 2.8: *Photograph of phantom S attached to the holder, mounted to the sample bed of the MARS scanner. Source and camera position not yet aligned with TLD chips.*

cedure is standardized, beginning with a preheat to 140°C over 10 seconds, then a gradual heating of the TLDs with temperatures increasing by 10°C per second up to 220°C after which it is kept constant for an additional 12 seconds. Final measurements of air kerma had multiple components of uncertainty; these were calculated using $SE_{\bar{x}} = \frac{sd}{\sqrt{n}}$ from the standard deviations of the readout values used to obtain each correction coefficient. The various components were added in quadrature as percentage errors according to the following formula (noting that expanded uncertainty of k=2, or 95% confidence interval, is twice this value):

$$E = \sqrt{E_{cal}^2 + E_{rel}^2 + E_{process}^2} \tag{2.5}$$

E_{cal} is the uncertainty in the energy calibration coefficient; E_{rel} is the uncertainty in the individual response correction coefficients; $E_{process}$ is the uncertainty in the readout process correction coefficient. The uncertainty of the background reading is typically ignored as the background value is nearly always a minute percentage

of measured values. For the experiment, the measurement uncertainty was found to be 1.8%, and an expanded uncertainty of 3.5%.

Results

Ganet's measurements showed that air kerma at the centre of each phantom was **17.2 ± 0.6 mGy** for phantom S and **18.2 ± 0.6 mGy** for phantom F. As for the depth dependency of dose, a slightly unusual result was seen as shown in figure 2.9.

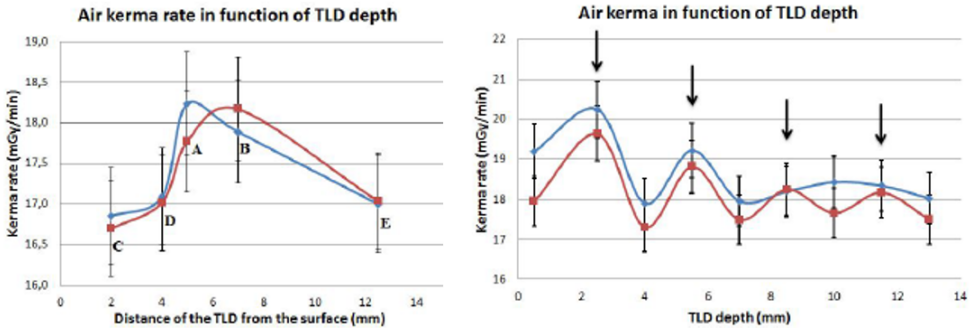

Figure 2.9: *Plots of air kerma rate against TLD depth, from two scans. Left - phantom S result. Right - phantom F result.*

Instead of a simple decreasing relationship between air kerma and depth within phantom, the TLDs appeared to exhibit oscillatory readings with depth. Because the higher readings generally came from TLD positions starting closer to the source, it was suspected that the cause of this behaviour was due to an initial beam-on time before gantry rotation and acquisition began - used as an X-ray stabilization period. An exception is perhaps chip position B in phantom S, which by that logic should not have a reading much different than the reading from position D. Here it is likely that Ganet made a systematic error in the rotational placement of the phantom relative to the source.

2.4 Review

To summarize the key points of this chapter:

- In collaboration with Dr. Nick Cook from Christchurch hospital, Ganet created and tested a dosimetry procedure and accompanying equipment for measuring CTDI in the MARS pre-clinical scanner using an Unfors ion chamber.
- In collaboration with Dr. Sophie Walker and Dr. John Laban from NCRS, Ganet created and tested a dosimetry procedure and accompanying equipment for measuring air kerma in the MARS pre-clinical scanner using TLDs.
- First estimates of scan dose were obtained.
- Ganet's results identified aspects of the scanner behaviour which contributed to irregular radiation dose patterns.

The overarching project aims to provide the rising MARS imaging modality with a thorough consideration for dosimetry. Ganet's study has strengthened links with collaborating partners, bringing together a wide range of expertise to demonstrate the application of classical dosimetry techniques to the MARS scanner. In turn, this would form the baseline for future dosimetry systems directly utilizing spectral detection - heralding a potentially personalized approach to dosimetry.

The collective experience gained from Ganet's work provides a stepping stone to the next stage of dosimetry for MARS - one which hopes to consider dose deposition beyond the simple case of generic phantoms. Techniques formulated by Ganet serve as a baseline of comparison for more complicated dosimetry techniques such as Monte Carlo simulation, as described in the following chapter 3. While Ganet's techniques were largely adopted for experimental verification of these simulations, modifications were incorporated to address specific issues. Most prominently, the irradiation due to initial beam-on seen in Ganet's TLD measurements can be viewed as unnecessary. Furthermore, Ganet's procedure of using the Unfors Raysafe ion chamber with the MARS scanner was deemed unsafe due to the requirement of removing covers and running a cable through moving components. Details on how these issues were addressed are covered in chapter 4.

Chapter 3

Monte Carlo simulation of pre-clinical MARS scanner

3.1 Overview

Monte Carlo simulation is regarded as the gold standard of dose evaluation tools. Assuming correct implementation and sufficient verification, advanced Monte Carlo codes boast the ability to quantify dose with high spatial precision.

This chapter introduces the concepts of Monte Carlo simulation, and presents the development of a simulation based on the small bore MARS scanner. In addition, preliminary simulated estimates of dose are compared with various alternative calculation methods; this functions both as initial order of magnitude verification and speculation of future on-board dosimetry algorithms. The final part of this chapter presents a preliminary method of importing DICOM (Digital Imaging and Communications in Medicine) format images from MARS scans into the Monte Carlo simulation as material volumes for retrospective spatial dose mapping.

Recognition is given to colleagues Marzieh Anjomrouz and Muhammad Shamshad for their previous work in characterising the MARS scanner X-ray source beam profile, and sharing of simulation data for cross comparison.

3.2 Introduction to Monte Carlo

Monte Carlo method is a class of mathematical calculation which uses random sampling to solve physics, mathematics and economics modeling problems of a stochastic nature. At a rudimentary level, flipping a coin many times to find the probability of landing heads or tails can be considered solving a problem with random numbers. While seemingly simple, this idea can be applied to the more complex problem of radiation transport and dose deposition in matter. After all, the interaction of radiation particles with matter also happens to be stochastic in nature as discussed in chapter 1.

For an X-ray beam incident on an irregular object, knowing the amount and location of energy deposition would involve:

1. Tracking the position and momentum of all photons as they travel through space,
2. Evaluating the probability of interaction with matter at each microscopic step,
3. Further tracking possible resultant secondary particles or scattering,
4. Repeating until there are no further interactions, the particle drops below an energy cut-off, or has exited the system.

With endless branching possibilities, purely analytical approaches are not considered to be feasible for many radiation transport problems. Yet with modern computational capabilities, Monte Carlo offers a way to repeatedly simulate particle tracks a large number of times in a short period. With a sufficient number of simulated particles, or 'histories', the statistical uncertainty can be minimised and a confident estimate of desired information can be obtained [Kalos and Whitlock, 2008].

There are many Monte Carlo software codes for radiation transport in medicine, such as EGSnrc [Kawrakow and Rogers, 2003] and GEANT4 [Agostinelli et al., 0038]. In general their process follows these basic steps:

1. Define set of inputs and constraints for a system, and a quantity to be scored
2. Randomly generate a series of inputs into the system and perform computation

3. Amass the subsequent set of scored outputs and aggregate into a final result

The first step may include defining coordinates and boundaries of virtual space, constructing geometries, choosing and placing particle sources, and selecting scored quantities. How these parameters are set in the simulation varies with the code, with some like EGSnrc offering simple graphic user interfaces (GUI) to select from a limited range of options; others like GEANT4 allow greater customization at the price of simplicity.

The progression followed during a simulation again depends on the code, on how particles behave and how they react to matter of specified characteristics. Physics lists employed by each Monte Carlo code contains the required information on material properties, interaction cross section and more.

Often, codes include methods of attaining greater statistical precision for a lower number of histories. This is called variance reduction [Kalos and Whitlock, 2008], and generally they focus on cutting computational effort to aspects of a simulation deemed less important for the particular application and emphasizing certain aspects deemed more important. For the scenario of X-ray generation through bremsstrahlung, because the efficiency of photon production is low a large amount of computational time is wasted tracking inconsequential electrons. Techniques such as 'particle splitting' or 'forced interaction' help offset this by forcibly increasing the photon yield and hence increasing the simulation statistical efficiency. These techniques also incorporate self-corrections to offset the numerical boost in output; increasing the number of bremsstrahlung photos produced by 1000 times will not increase the resultant dose by 1000 times. Other techniques like 'importance sampling' aim to focus on the tracking of a specified subset of particles while those less important may be abandoned entirely, as in 'Russian roulette' [Kalos and Whitlock, 2008].

GEANT4

GEANT4, or GEometry ANd Tracking, was developed at CERN (Geneva Switzerland) addressing a need for a robust versatile simulation software tool. GEANT4 is capable of handling the modeling of modern particle and nuclear physics of the level of complexity seen in high energy physics experiments (eg. Large Hadron Collider experiments). After initial release, the toolkit was further maintained and refined by the GEANT4 collaboration which to this day provides user support and

updates. The current version of GEANT4 is open source, free, and having applications broadening well beyond the original purposes of high energy physics to medical, and even space applications. GEANT4 is capable of simulating a wide range of particles from electrons, photons, protons and neutrons to heavy charged particles - from eV scale energies upward. Motion and timing functionality is also possible, which is useful when simulating the mechanisms of dynamic systems like a CT scanner. The versatility of GEANT4 can scarcely be emulated with other Monte Carlo codes [Agostinelli, 2003] [Allison, 2006].

In contrast to most other codes however, GEANT4 is less a user orientated package and more of a developer orientated kit-set. While boasting the greatest flexibility and potential for varied applications, technical programming expertise is a barrier for many users. Consequently many user codes have arisen aiming to offer user-friendly packages overlying GEANT4, such as GATE [Buvat and Lazaro, 2006] and TOPAS [Perl et al., 2012]. These platforms take advantage of the vast databases provided by GEANT4, while reducing or removing the programming skill requirement. For the work in this thesis, TOPAS was chosen for use in simulation to aid in reducing development time.

TOPAS

TOol for PArticle Simulation, or TOPAS, was first developed from GEANT4 to address a need for non-complex Monte Carlo tool for proton therapy simulations [Perl et al., 2012]. The initial design of TOPAS specialised in refining features relevant to proton therapy simulation, such as geometric components and physics settings. However, the innovative parameter control system aimed to retain the flexibility of the underlying GEANT4 code. This foresight paved the way for TOPAS to become a general tool for all areas of radiation therapy and even imaging.

The parameter control system allows users to define all aspects of their simulation using a comprehensive system of parameter syntax, written in text files. This is in contrast to direct GEANT code which requires C++. The user can specify geometry setup, particle source setup, scoring setup, physics settings, variance reduction, graphical settings, and so on. While integrating the geometric shapes database provided by GEANT4, TOPAS also includes its own variants capable of spatial subdivision (further discussed in section 4.4.1). Furthermore, importing geometry data from CAD (computer aided design) and DICOM format is supported.

As of version 2, TOPAS does not yet include a GUI so it is run through the command line. Quantities of interest can be directly display within the console, but for more complicated or large outputs data is generally given as spreadsheet values of scored quantities, indexed by the various parameters chosen (e.g. Particle energy, coordinate numbers). It is up to the user to analyse and display this information accordingly.

TOPAS was the tool of choice for this study on account of its unrestricting capabilities, and relative simplicity. It enjoys the benefits of GEANT4's freedom in defining simulations, while avoiding many of the technical challenges. This gives TOPAS an edge in dosimetry simulations for CT imaging compared to codes such as EGSnrc. Moreover, TOPAS is quickly becoming the standard tool used by the Medical Physics division at University of Canterbury and boasts dedicated user support and active online community. As it is intended for TOPAS to evolve into a universal tool for medical physicists, expansion of applications have been welcomed and developers readily tailor the toolkit to user needs while regularly incorporating advancements in GEANT4. During work in this thesis, communications via the online user forum has been a useful source of advice from both developers and fellow users. Correspondingly some issues encountered during this study were conveyed to the developers, contributing to bug fixing and accelerated improvement in variance reduction for secondary particles and geometric particle scoring.

3.3 Modeling of the MARS scanner X-ray source

3.3.1 Procedure

For the development of a Monte Carlo simulation of radiation dose, it is logical to begin at the radiation source. The source unit used by the MARS scanner was the model SB-120-350 manufactured by Source-Ray Inc. This first task involved writing the TOPAS simulation file defining the X-ray source, then running the simulation to obtain information on both the spatial distribution and spectral composition of the produced photons. The results were then compared with the standard reference SpekCalc [Poludniowski and Evans, 2007], as well as with similar simulations run by Anjomrouz and Shamshad using BEAMnrc [Anjomrouz and Shamshad, 2015]. BEAMnrc is an application within the EGSnrc code, and part of the GUI is shown in figure 3.1. These comparisons served

as reassurance TOPAS can produce approximately expected results under these basic conditions, as well as cross verification. Parameters used to define an X-ray

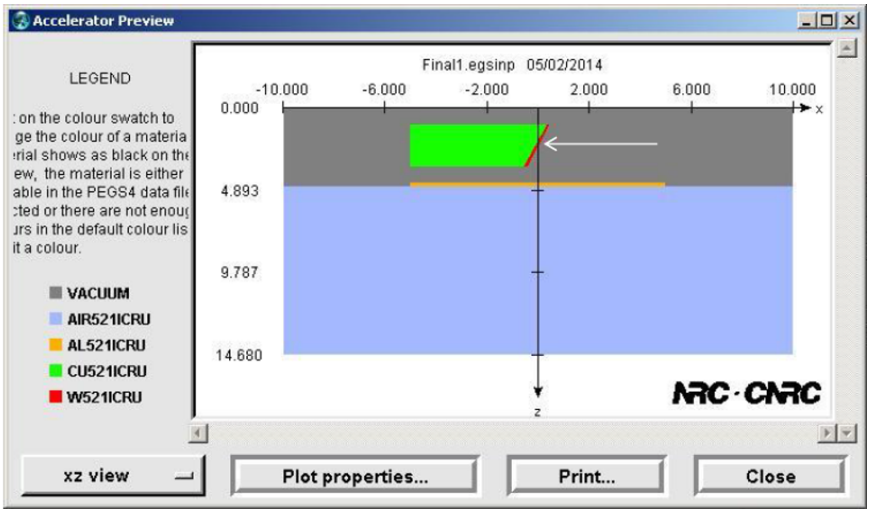

Figure 3.1: *Part of the GUI for BEAMnrc, showing simulation of the MARS X-ray tube [Anjomrouz and Shamshad, 2015].*

source was based on specifications found in the manual of the X-ray source used by the current small bore MARS scanners [Manez, 2012]. Figure 3.2 shows a schematic drawing of the X-ray tube arrangement within the source unit taken from the manual. Additional information indicated the target was a 1 mm layer of Tungsten on Copper body, an anode angle of 20°, inherent filtration at 120 kVp equivalent to 1.8 mm Aluminium and a focal spot of 0.073 mm.

Based on the specifications, a simulation X-ray tube was planned. However, instead of including all components such as the glass casing with vacuum and surrounding oil coolant, all inherent filtration components were simplified into one layer of filter that included any additional filtration. The cathode filament was also substituted in the simulation for a pure mono-energetic electron source with flat spatial distribution and circular width matching the specified focal spot size. The geometric components representing the anode target and body were defined through the shapes database, allowing selection of dimensions and angle.

The main parameters for producing X-ray spectra with the 3 available methods are summarised below:

- Cathode represented by 120 keV mono-energetic electron beam with a spot size of 0.07 mm (and hence an X-ray source of 120 kVp)
- 1 mm thick Tungsten anode target at 20° angle
- Inherent filtration represented by 1.8 mm of Aluminium
- 11 cm source to scorer distance (in air)
- 70x70 mm square scoring plane
- 2 billion histories
- Variance Reduction technique applied to secondary particle generation, splitting number of 1000

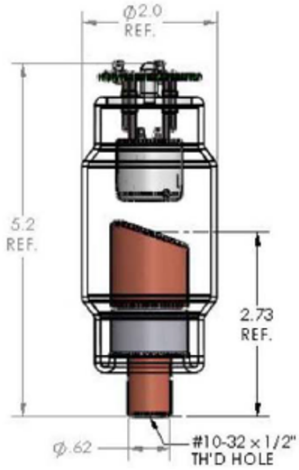

Figure 3.2: *Diagram of X-ray tube used in the source unit [Manez, 2012].*

The basic X-ray source simulation is shown in figure 3.3. Within the simulation, a 70x70 mm scoring plane was defined 11 cm from the focal spot of the anode to record the energy and position of photons generated from 2 billion histories. The g4em−standard_opt3 physics option was chosen by default, and 'Secondary Biasing' variance reduction method selected to split bremsstrahlung products by 1000.

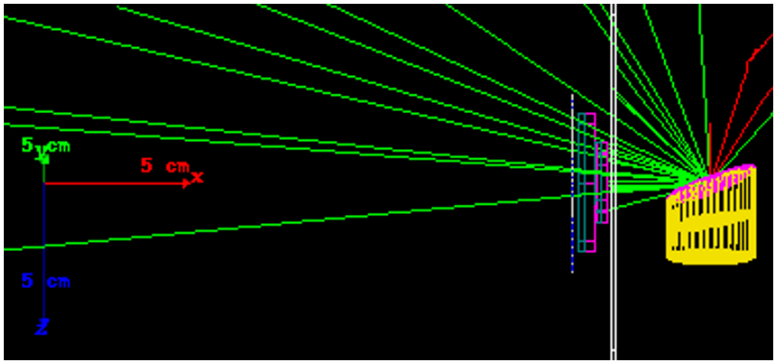

Figure 3.3: *Graphical OpenGL output from TOPAS simulation of X-ray source. Components shown are the tungsten and copper anode in yellow/pink, the Al filter in white, tungsten and Aluminium collimators in dark green/purple, photons in light green, and electrons in red.*

3.3.2 Results and analysis

In this study, MATLAB was used and scripts were written to read and convert TOPAS output files into specific plots depending on the type of scoring used.

Figure 3.4 shows that the TOPAS simulation produces an X-ray spectrum which matches the shape of that produced by a similar BEAMnrc simulation, as well as the SpekCalc results. Because SpekCalc gives values in units of counts/keV/mAs/cm^2 at 1 m, it was converted to equivalent units by accounting for the inverse square law to find counts at 11 cm, conversion of area (mm) and conversion of current (μAs).

Aside from spectral verification, spatial cross checking was also done. In this case, TOPAS was only compared with BEAMnrc. Figure 3.5 shows the beam intensity on a 70x70 mm scoring plane, comparing the two Monte Carlo codes for photons in four energy ranges: all photons, photons below 40 keV, photons between 40-80 keV, and photons higher than 80 keV. The comparison shows that TOPAS and BEAMnrc give very similar photon distribution where higher energies have a slightly greater presence on the left and lower energies incline towards the right side. This can be explained by the heel effect, where self-attenuation within the Tungsten anode target has a greater effect on the less penetrating lower energy photons. Photons generated within the target must travel a greater distance within solid Tungsten to reach the anode side of the scoring plane, which is why

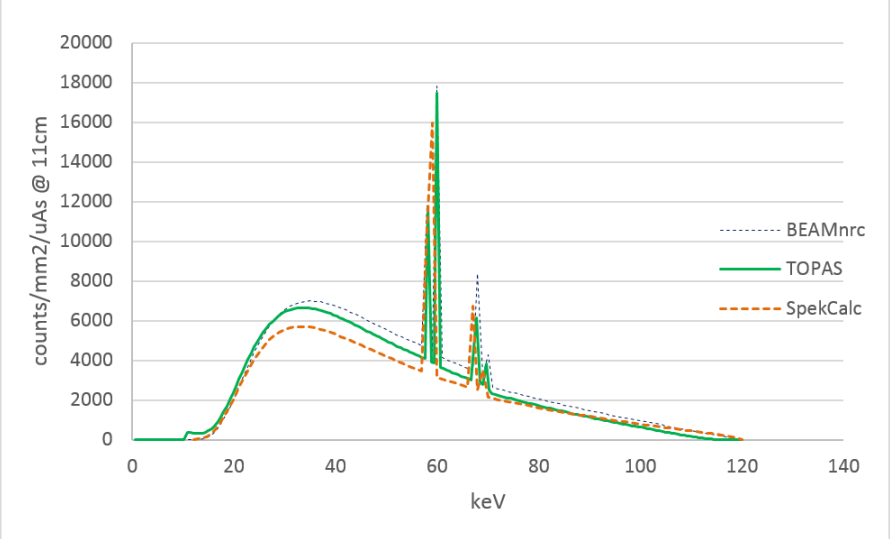

Figure 3.4: *Plot of the X-ray spectrum of the source modeled by TOPAS compared with SpekCalc and also add BEAMnrc result. The Monte Carlo code output is given in units of counts/mm^2/μAs at 11 cm.*

there is greater low-energy and overall beam intensity towards the cathode side of the scoring plane. Penetrating higher energy photons are less susceptible to self-attenuation and hence exhibit less of the effect.

There are however, noticeable differences in the comparisons. The SpekCalc spectrum shown in figure 3.4 appears to be lower than the two Monte Carlo spectra at all energies below about 80 keV. It also fails to distinguish between the two characteristic peaks near 60 keV. Any comparison with SpekCalc needs to be treated with caution, especially since SpekCalc does not account for scatter contributions. Also, it only accounts for photons near central beam axis.

More subtly, there is also a near-consistent difference in counts between BEAMnrc and TOPAS simulations above 30 keV. Figure 3.6 shows a closer inspection of the difference in output between the two simulations. Using the beam brightness distribution data used in figure 3.5, line profiles were taken horizontally along the centre of each brightness plot. Also, the Pearson product-moment correlation coefficient between the beam brightness plots of the two Monte Carlo codes was calculated using the MATLAB function *corr2*. Furthermore, the percentage difference in counts over the entire scoring plane was calculated.

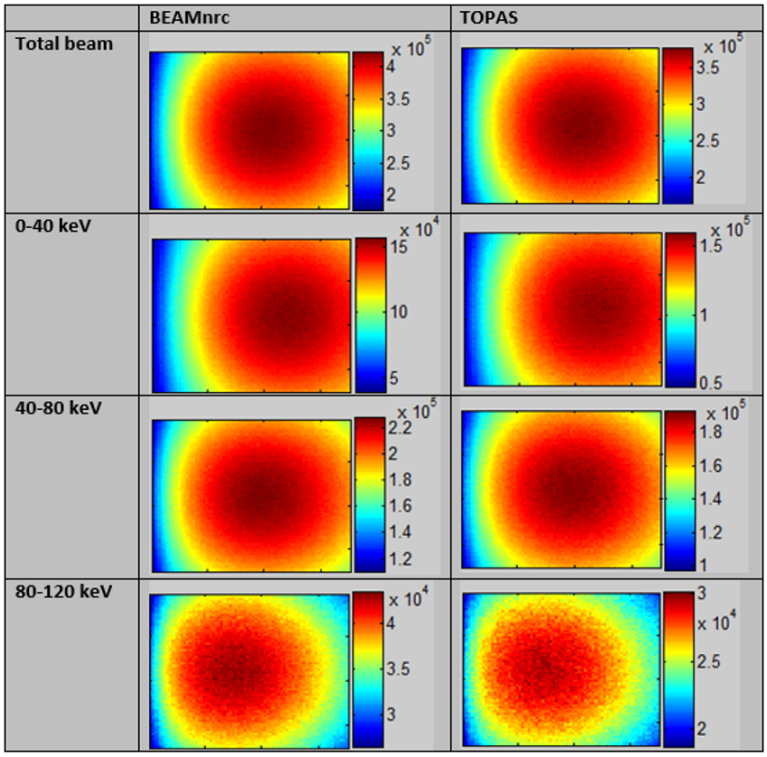

Figure 3.5: *Comparison between TOPAS and BEAMnrc in simulating X-ray generation. Plotted are counts/mm^2/μAs on 70x70 mm scoring planes at 11 cm from source.*

Here it is again confirmed that the difference in counts is mainly at the higher energy ranges, reaching as high as 31% disparity above 80 keV. These observations are consistent with the difference in counts observed in figure 3.4. Though it is suggested by the near-unity correlation coefficients that despite a difference in counts, the spatial distribution pattern of these counts are very similar between the two Monte Carlo codes. The exact cause of the mismatch in magnitude of counts may be related to the physics settings between the two Monte Carlo codes, or subtle differences in implementation of the simulation parameters. Such differences are a subject for further study.

Shamshad and Anjomrouz had also attempted to use the Cadmium Telluride Medipix3RX detector within MARS scanner 11 to measure the photon spatial

	Horizontal line profile, BEAMnrc vs. TOPAS	% difference in counts	Correlation coefficient
Total beam	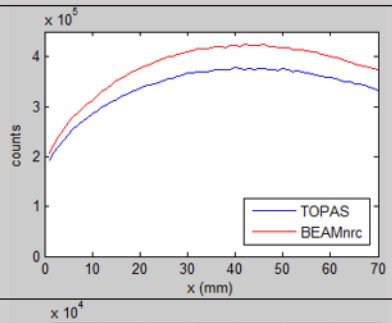	**10**	**0.9995**
0-40 keV	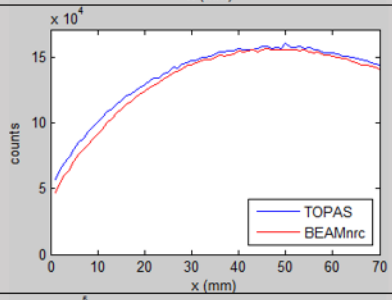	**3.4**	**0.9993**
40-80 keV	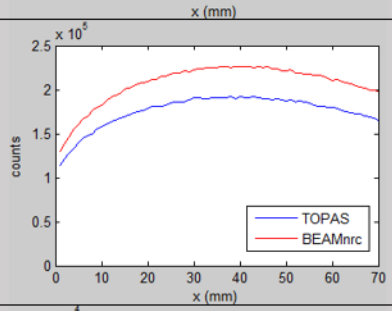	**15**	**0.9982**
80-120 keV	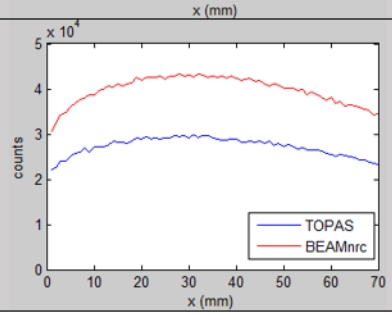	**31**	**0.9836**

Figure 3.6: *Horizontal line profiles based on the photon distributions in figure 3.5. Also shown are percentage difference in counts between the two Monte Carlo codes and the Pearson product-moment correlation coefficient for each energy range.*

distribution. They found measured counts were $5-12\%$ (even more when considering uncertainties) lower than simulated counts depending on position. This is likely to do with physical processes taking place within the detector, causing signal distortions which negatively impact its detection efficiency. Thus it is difficult judging what the 'correct' source output is.

In general, the output of TOPAS shows conformity with expectation. The spectrum shape of the X-rays broadly agrees with SpekCalc and BEAMnrc simulation, while the spatial distribution is also similar between the two Monte Carlo codes. The subtle dissimilarities in spectrum and difference in higher energy counts remain difficult to explain at this stage.

3.4 Comparing TOPAS with alternative calculation methods

With the assumption that the X-ray source simulation produces photons with reasonable spatial and spectral distribution, the next question to ask is whether the simulation can score dose correctly. Partly in order to satisfy this question and partly as an early investigation into how a future 'on-board' dosimetry system for MARS might work, non-Monte Carlo methods of dose calculation were explored. This section describes a basic test of the reliability of dose scoring in TOPAS, and two methods of estimating dose to simple objects given information about the incident radiation.

$$simulatedDose = \frac{rawDose}{N} \times I \times t \times 6.241508 \times 10^{18} \frac{e}{C} \tag{3.1}$$

For enabling comparison between Monte Carlo results and other methods, equation 3.1 was used to convert simulation values such that the number of histories N scaled to the expected number of X-ray source particles in a true scan of time t and tube current I.

3.4.1 Simple test of TOPAS dose scoring

Before embarking on more complex dosimetry simulations with TOPAS, assurance is needed that the code is fundamentally capable of giving reasonable estimates of dose from X-rays. For the basic scenario of a set number of photons being completely absorbed by a known volume of water, a simulation was run on

TOPAS and compared with a simple calculation of dose.

Simulation: TOPAS code was written to define a water box of 0.2x0.2x0.2m with a photon source at its center emitting 10 keV photons. No photons were expected to escape absorption by the volume. This was run for 200 histories (note that histories here equivalent to number of source particles) and the dose to water was scored. The total dose scored was **4.0054x10^{-14} Gy**.

Calculation: For dose (Gy) in Joules per kilogram: Energy (Joules) = 10 keV $\times$ 1000 eV/keV $\times$ 1.60218$\times$10^{-19} J/eV $\times$ 200 histories = 3.20436$\times$10^{-13} J

Mass (kilogram) = (0.2 m)^3 $\times$ 998.2 kg/m^3 = 7.9856 kg (at room temperature) or (0.2 m)^3 $\times$ 1000 kg/m^3 = 8 kg (at 4°C)

Dose (Gray) = Energy/Mass=**4.11575$\times$10^{-14} Gy** (at room temperature) or **4.00545$\times$10^{-14} Gy** (at 4°C)

Comparing the TOPAS simulation with the calculation assuming 4°C is a close match with only a minute difference. This demonstrates that at a fundamental level TOPAS can accurately score dose. It is interesting to note though that the temperature assumed by the scoring is a closer match to 4°C than at room temperature, which results in a difference scored dose by more than 2.5%. This may be an issue requiring consideration at a later stage, especially considering live samples will have a body temperature even higher than room temperature.

3.4.2 Calculation of fluence and kerma

Following on from the first test, another approach to estimating the dose is through calculation of the collisional kerma. Given knowledge of the source beam and tabulated values of mass energy absorption coefficient of dry air from NIST [Hubbell and Seltzer, 2015], the collisional kerma can be calculated from the following equation [Podgorsak, 2005]:

$$K_{col} = \Psi(\frac{\mu_{en}}{\rho}) = \Phi E(\frac{\mu_{en}}{\rho}) \tag{3.2}$$

Here K_{col} is the collisional kerma, Ψ is the beam energy fluence, Φ is the photon fluence, and $\frac{\mu_{en}}{\rho}$ is the mass energy absorption coefficient of the attenuation material. While it is not strictly radiation dose, collisional kerma is a measure of X-ray energy deposition. In a way it represents the radiation exposure in a point

in (an air filled) space independent of an irradiated object.

This concept was first trialed on the simple scenario of a flat mono-energetic photon beam, then on the X-ray source defined previously. In both cases the calculated result was compared with TOPAS simulation of absorbed dose under similar parameters.

Simple kerma exercise

In the scenario used here, we have a mono-energetic 54 keV photon beam 1x1 cm wide containing a million particles. 54 keV was chosen as it is close to the weighted average energy of a 120 kVp X-ray spectrum with 3 mm Al filtration. Following the above equation for kerma, the expected fluence would be Φ**=1,000,000/cm^2, E=8.65$\times$10^{-15} J**, and according to NIST database the mass energy absorption coefficient of dry air at sea level for 54 keV photons is $\frac{\mu_{en}}{\rho}$ **= 3.555$\times$10^{-2} cm^2/g**. Hence the expected value for air kerma in this scenario would be **3.08$\times$10^{-7} Gy**.

A TOPAS simulation of this scenario, the beam is directed at a box of 1x1x2 cm (2 cm along the direction of the beam). Scoring for dose within the box gave **1.28x10^{-7} Gy** if the box was composed of air, and **2.85x10^{-7} Gy** if it was composed of water.

We can see that while the results are the same order of magnitude, the much lower dose seen in the air box reflects the lack of build-up which causes dose to differ from kerma by a greater amount. There is greater agreement between the water-box dose and the expected kerma as the greater attenuation of water means the build-up takes place over a much shorter distance compared with air, but the lower end value reflects the missing dose as a result of a build-up region.

Application to a MARS scan protocol

Here, the approach is extended to an irradiation scenario based on a true MARS scan protocol popularly used within the team. Parameters relating to the irradiation conditions are as follows:

- X-ray source model as described in section 3.3, with 120 kVp tube voltage and 37 μA tube current

- 0.375 mm additional Cu filter on top of 1.8 mm Al inherent filtration
- 129.6 s irradiation time (based on 720 frames per rotation, 150 ms exposure time plus 30 ms readout per frame, and a single gantry rotation)
- Irradiated object is a 20x10x10 mm water-box (20 mm along beam axis)
- 220 mm SOD (source to object distance)

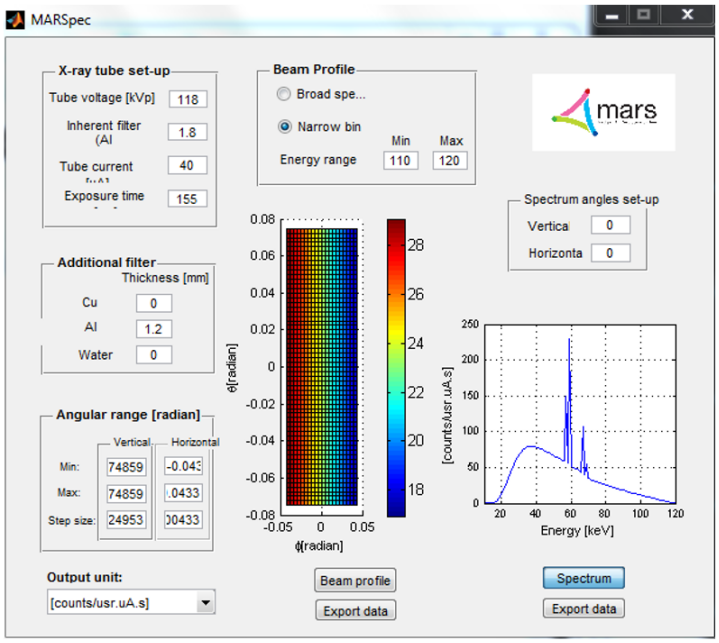

Figure 3.7: *GUI for MARSpec by Anjomrouz and Shamshad.*

To help with obtaining values of fluence for this task and the next task, software called MARSpec was used. This program was developed by Anjomrouz and Shamshad based on their BEAMnrc simulation data [Anjomrouz and Shamshad, 2015], and boasts similar capabilities to SpekCalc in spectrum calculation and the GUI is shown in figure 3.7. In addition, the program is able to output plots of beam intensity as a function of filtration, energy, and solid angle range. Because of the convenience it provides, and because it was previously shown that the various X-ray source models are reasonably consistent with each other, it was decided that MARSpec be used for the remaining work in this chapter. Fluence was found by MARSpec to be **1888 counts/μSr/μA/s** at the central beam axis.

Converting area to steradians we find a 10x10 mm square area is the equivalent to **2066** μ**Sr**.

To simplify the kerma calculation, some approximations were made. Shown in figure 3.8 is the X-ray spectrum resulting from the above listed specifications. Because mass energy absorption coefficients ($\frac{\mu_{en}}{\rho}$) are a function of photon energy, a representative value for energy is needed. Taking the weighted mean of the spectrum, we get the value **65.8 keV = 1.05423**$\times$**10**$^{-14}$ **Joules**, and using linear interpolation on the available NIST database values for ($\frac{\mu_{en}}{\rho}$) of dry air we get $\sim$**2.77**$\times$**10**$^{-2}$ **cm**^{2}**/g** for 65.8 keV photons.

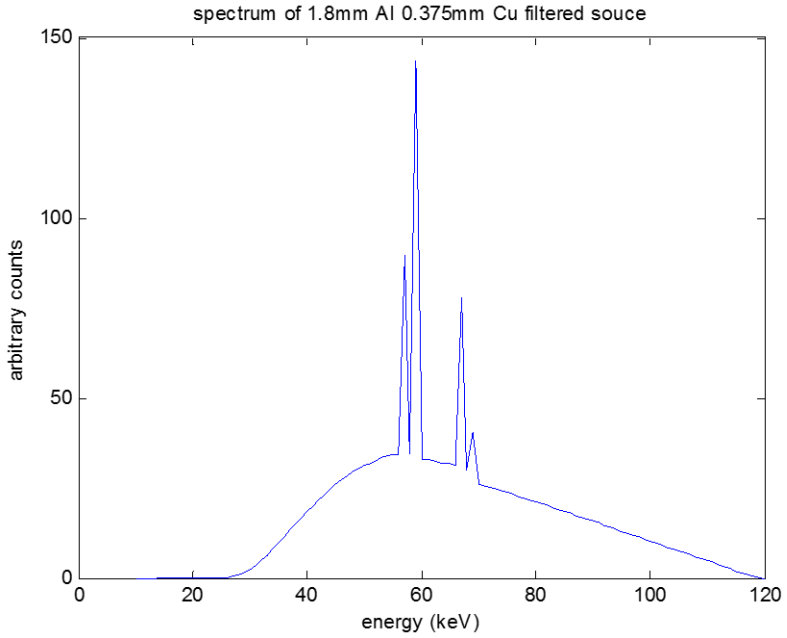

Figure 3.8: *0.375mm Cu and 1.8mm Al filtered source using MARSpec.*

The calculation estimates a collisional kerma for this ideal exposure of: 1888 counts/μSr/μA/s $\times$ 2066 μSr/cm^2 $\times$ 1.05423$\times$10^{-14} J $\times$ 37μA $\times$ 129.6 s $\times$ 2.77$\times$10^{-2} cm^2/g $\times$ 1000 g/kg = **5.46 mGy**

A simulation using these parameters on TOPAS scored 1.62$\times$10^{-11} Gy for 85$\times$10^6 histories. Correcting this for the intended number of source particles: 1.62$\times$10^{-11} Gy $\div$ 85$\times$10^6 histories $\times$ 37$\times$10^{-6} A $\times$ 129.6 s $\times$ 6.241509$\times$10^{18} /Coulomb = **5.7 mGy**.

The two values are remarkably close given the approximations made. Of course the two values were not expected to match exactly considering that the collisional kerma calculation doesn't address a change in fluence as the beam is attenuated within the object, as well as inherent differences between kerma and absorbed dose. It should be noted that the scoring quantity was chosen to be 'absorbed dose to water' as TOPAS did not come with a dedicated kerma scoring functionality. However, TOPAS supports custom implementation of scorers such as kerma, and indeed creation of kerma scoring functionality has been reported by other groups within the TOPAS user community.

3.4.3 Calculation of dose by ray line attenuation

This method of estimating dose was formulated from speculation on how a future on-board MARS dosimetry system may work. If a MARS scanner was capable of accurately measuring the beam profile - the spectrum and spatial distribution of photons - then information could be obtained on *how much* attenuation is experienced by each ray passing through an object. Also, because an ideal spectral scan can tell us the material and structural composition of an object, there appears to be enough information to infer *where* radiation is attenuated. Assuming that scattered photons have a relatively small influence on dose deposition, this could potentially be a computationally non-intensive way to map the dose deposition in 3D.

In a basic approach to this idea, we first imagine a situation where the object is known and the source beam is known. For the object we use a water cylinder 30-35 mm in diameter and 100 mm in length, and for the source beam we follow the profile generated by MARSpec. The Beer Lambert law can then be applied to calculate the amount of attenuation experienced by a set of 'ray lines' passing through the object, and hence provide a first approximation to the absorbed radiation:

$$I_E = I_{E0} exp^{-\mu_E^m L_m} \tag{3.3}$$

Here, the beam of intensity I travels a path length L through material m of linear attenuation μ – all for a beam of energy E. This calculation was done using MATLAB, and the process of determining each variable in the equation are described as follows:

1. Finding L: By discretising the beam-front into a grid of angular pixels,

path length L of each 'ray' through the cylinder can be calculated with trigonometry such that $L = L(\phi, \theta)$ for discrete values of ϕ and θ. Given that the central ray will experience a path length through the cylinder of d_0, variation in path length with horizontal angle ϕ varies by a factor $x(\phi) = \frac{1}{(cos(\phi))}$ (see figure 3.9). In addition, path length with vertical angle θ varies by a factor $y(\theta) = \frac{\sqrt{(r^2 - SOD^2 tan^2(\theta))}}{r}$ (see figure 3.10). The last equation assumes that SOD is sufficiently large and θ sufficiently small that all ray lines can be considered traveling horizontally through the phantom.

2. Finding I_{E0}: For the each of the angular pixels, the number of photons of each energy are given by MARSpec. These were divided into bins of 10 keV so we have the number of photons in a 'ray' between $10-20$ keV, $20-30$ keV, ..., $110-120$ keV. Note that MARSpec gives values in units of counts/μSr/μA/s, which needs to be converted into counts/'angular pixel' by using scan and geometric information.

3. Finding μ_{mE}: For each of the energy bins, the mass attenuation of water was taken from NIST [Berger et al., 1998] where the representative value of each bin was its central energy (so for the 10-20 keV bin, the mass attenuation was chosen for 15 keV). These were converted to linear attenuation through multiplying by the density of water at room temperature 998.2 kg/m^3.

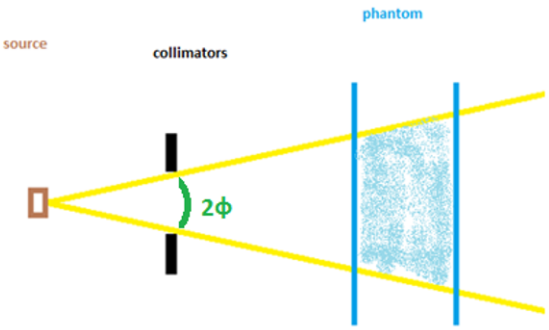

Figure 3.9: *Schematic of collimated beam traveling through the sample cylinder, viewed from above. The horizontal angle is shown.*

This way, I_E in the Beer Lambert equation can be calculated for each 'ray line' through the water cylinder at every energy bin. The difference between

initial beam intensity I_0 and intensity I after passing through the object, was treated as the set of photons which have deposited their entire energy into the sample.

$$Dose(CTDI) = \frac{\sum_E (E \times (I_{E0} - I_E))}{cylinderMass} \div sliceWidth \times cylinderLength \quad (3.4)$$

Dose is defined as energy deposited per mass, given in units of Gray (Joules per kilogram), and so the total energy treated as absorbed by the cylinder can be divided by the mass of the exposed portion to give an approximation to the dose.

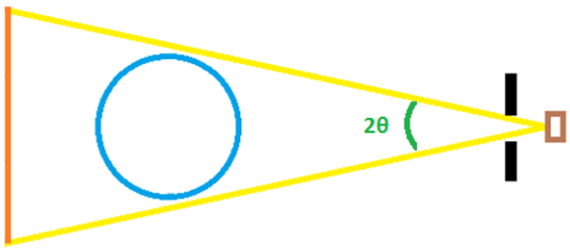

Figure 3.10: *Schematic of collimated beam traveling through the sample cylinder, viewed from the side. The vertical angle is shown.*

This approach was tested with two exposure conditions, both based on MARS scan protocols.

Application to MARS scan protocol

As with the kerma calculation method, the ray-line approach was tested on irradiation conditions matching the true MARS scan protocol. The parameters of irradiation are essentially identical to that listed in section 3.4.2 but with some modifications:

- Irradiated object a water equivalent cylinder 35 mm in diameter and 100 mm in length
- Vertically aligned detector array of thickness 14 mm at ODD = 50 mm

- Collimation of the beam for the detector such that slice thickness is 11.4 mm wide on average (length of cylinder irradiated, see figure 3.9)
- 120 kVp tube voltage
- 37 μA tube current
- 0.375 mm additional Cu filter on top of 1.8 mm Al inherent filtration
- 129.6 s irradiation time (based on 720 frames per rotation, 150 ms exposure time plus 30 ms readout per frame, and a single gantry rotation)
- SOD =220 mm

Using the above described ray-line dose calculation, the result calculated with MATLAB was **30.8 mGy** CTDI. A simulation run on TOPAS with matching irradiation conditions gave: 2.5204×10^{-12} Gy $\div$ 83.2×10^{6} histories $\times$ 37 μA $\times$ 126 sec $\times$ $6.241509\times10^{18} e/C \div$ 11.4 mm $\times$ 100 mm = **7.73 mGy** CTDI.

Additional MARS scan protocol

As another test of this dose estimation approach, an irradiation scenario was based off a MARS scan protocol made for the experiments described in chapter 4. This protocol will henceforth be referred to as the base protocol. In this protocol, the following parameters were used:

- 40 μA tube current
- 130 ms exposure + 25 ms readout
- 360 projections/rotation (hence an ideal 55.8 s per rotation)
- 118 kVp tube voltage
- SOD = 200 mm
- ODD = 48 mm
- 2.8$-$3mm Al filtration (including inherent)
- Ideal slice thickness of 11.3 mm

The total dose found through MATLAB was **8.288 mGy**, and gives a CTDI of **34.8 mGy**.

A simulation run on TOPAS with matching irradiation conditions gave 1.0427 $\times 10^{-11}$ Gy $\div$ 83.2$\times 10^{6}$ histories $\times$ 40 μA $\times$ 55.8 sec $\times$ 6.241509$\times 10^{18} e/C$ 11.3 mm $\times$ 100 mm = **15.45 mGy** CTDI.

Remarks

Compared with Monte Carlo simulations, results of the ray-line attenuation calculations give significantly greater estimates of dose - more than double in fact. Reflecting on the assumptions made, this does not come as a huge surprise: we ignored the effects of scatter and reflection and assumed all attenuated radiation was absorbed. This alone would intuitively raise the dose estimation to higher than what it would be realistically. Also, the discretisation of the spectrum into 12 bins and having a linear attenuation coefficient value representing all photon energies within each bin could introduce a non-trivial amount of error. Though an average linear attenuation for an energy bin is a fair approximation at higher energies, at lower energies linear attenuation of water is incredibly sensitive to changes in energy. It is likely that an average linear attenuation for a low energy bin will not be representative.

In its current state, the ray-line attenuation methodology is inadequate for showing reliable estimates of dose. Should a future on-board dosimetry methodology be based on this approach, it would need to factor in the effect of scatter, and treat attenuation coefficient values as continuous rather than discrete. At such a stage, the spatial accuracy of dose mapping would need further verification with a more complete Monte Carlo simulation.

3.5 Spatial dose deposition scoring and importing DICOM

Previously described instances of dose scoring used standard scoring attached to physical geometry components, such as basic shape phantoms of a single material. While it has proved useful in estimating dose to specific phantom shapes and even the calculation of CTDI given the exposed slice thickness, the end goal will require scoring dose with high spatial precision – how much dose did one part of the object receive compared to another?

3.5.1 Scoring with spatial precision

TOPAS offers the capability to divide certain shapes into equal sized bins, which is useful in estimating how dose deposition varies within these objects. For example, spheres can be divided by angle of inclination, azimuthal angle and radius (ρ, θ, ϕ); cylinders can be divided by (r, h, θ); cuboids can be divided by (x, y, z). Dividable components are often sufficient in showing the behaviour of radiation energy within standard shaped single material phantoms.

For more complex objects than the dividable set provided by TOPAS, another method is needed for spatial scoring. Such objects may contain a multitude of different material components, and may come from CAD or DICOM import. This is important because in the future, we will need to be able to take *any* sample/patient image data scanned with MARS and use Monte Carlo simulation to accurately describe the spatial distribution of absorbed dose within.

The following demonstrates the capability TOPAS has for creating 'non-physical' parallel world components and using them to score in volumes which contain any physical components. Shown in figure 3.11 a water sphere was placed near the X-ray tube, but instead of scoring the particles with the sphere itself a parallel-world cube was also placed at that location. Because this cube exists in the 'parallel' world, there are no issues with overlapping volumes. Yet the cube still retains the capability to score particles traveling within it, even if the cube itself does not interact with them.

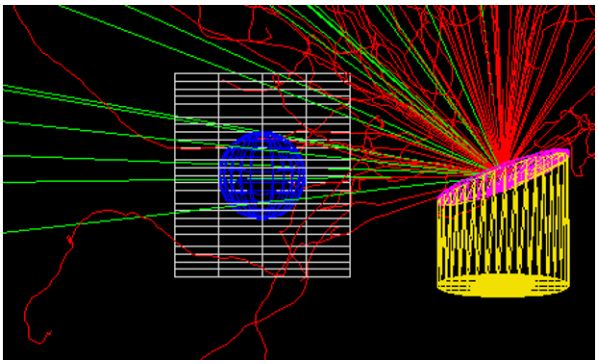

Figure 3.11: *TOPAS OpenGL visualization of X−ray tube irradiating a water sphere within a parallel scoring cube.*

The advantage of using parallel-world geometries is that if the shape of the

parallel world volume is chosen to be a dividable component, the scoring retains the ability to be divided. This is useful for customizing the coordinate system of scoring for any complex object. For the example in figure 3.12, scoring in Cartesian coordinates was applied to a spherical object. Though a complex object was not used in this example, the parallel cube enclosed both the water sphere *and* part of the surrounding air. Here we can observe the difference in energy deposition between the water sphere and the surrounding air, shown in figure 3.12. We even see the signs of attenuation, where the side of the sphere towards the positive X-axis direction receives greater radiation energy that diminishes with X (the source is placed at a higher X-coordinate).

As a result of parallel world scoring, the data given contains information akin to a 3D image - each voxel showing the radiation quantity scored. With this, it is even possible to have the image rendered as a visual dose map, such as that shown in figure 3.13. This figure displays the radiation exposure received by a cylinder in the scenario described in section 3.4.3 for a single gantry rotation. With improved methods of visualization, it would be feasible to overlay dose maps on top of CT renders similar to how radiation therapy treatment systems display their dose calculations.

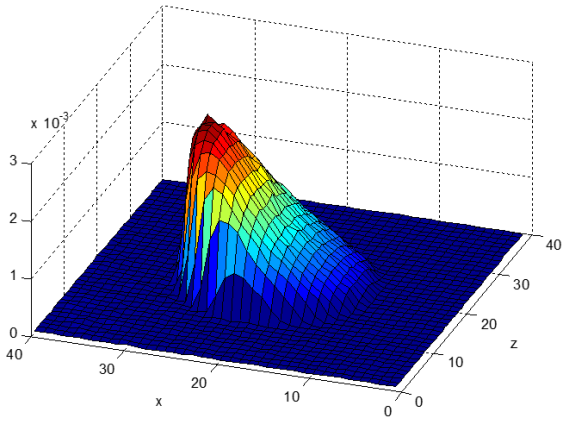

Figure 3.12: *MATLAB surf plot of the energy deposited summed in the x-z plane.*

Of course it is possible to increase the spatial resolution of scoring by increasing the extent of parallel component subdivision, but at finer resolutions the statistical noise becomes more evident. More simulation histories would be required for estimating dose with higher spatial precision.

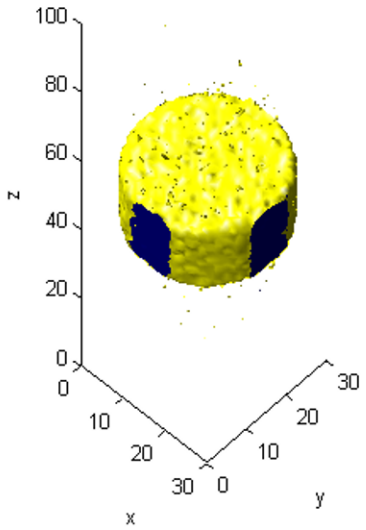

Figure 3.13: *MATLAB 3D visualization of the energy deposited into a cylindrical water phantom due to a single rotation exposure of the CT gantry. There is no intensity scale, a display threshold was used.*

3.5.2 Importing DICOM images for dose scoring

In estimating dose with TOPAS, the way to implement geometry varies with the complexity of the object and scoring. At one end of the scale, simple shaped phantoms can be represented by dividable components such as described previously. For slightly more complex shapes that do not exist in the basic shapes database, CAD may be required and parallel world scoring is needed. On the far end of the complexity scale is dose in patients; for this a typical approach is to use CT acquired DICOM images.

A strength of complex Monte Carlo platforms such as TOPAS is compatibility with data in DICOM format. Hence scanned objects can be imported into a TOPAS simulation for retrospective 3D dose analysis. Two sets of data from MARS scanning were used to test this capability: first a material calibration phantom used for a study of bone minerals, and second a mouse scan.

TOPAS version 2.1 uses a Hounsfield unit (HU) to material conversion algorithm based on a German study [Schneider et al., 2000]. For MARS scans however, instead of CT HU, tomographic data is given in multiple channels of

either X-ray energy or separated materials; the values are given in either 'effective linear attenuation' or spatial concentration in g/mL respectively. Thus before importing the two datasets into TOPAS, MATLAB was used to modify the data such that only one channel showing HU is present.

Material calibration phantom scan data

For the phantom dataset the energy channel representing the arbitration counter, or reconstruction using the entire spectrum was chosen and the units converted from linear attenuation to HU via equation 3.5.

$$HU = 1000 \times \frac{\mu - \mu_{water}}{\mu_{water} - \mu_{air}} \tag{3.5}$$

Here, μ is the linear attenuation given in the reconstructed image; μ_{water} is the linear attenuation of water; μ_{air} is the linear attenuation of air. The values of linear attenuation for water were taken from the portion of the image corresponding to a vial of water (figure 3.14) while that of air was assumed to be 0. The tomographic slice image of the phantom is shown in figure 3.15.

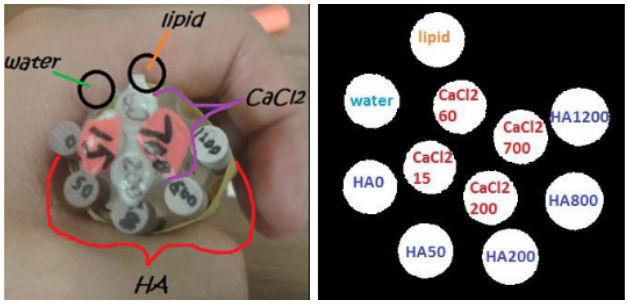

Figure 3.14: *Material calibration phantom used in a past study. Contains water, lipid, various aqueous solutions of CaCl (units of mg/mL), and various solid resin rods containing Calcium hydroxyapatite (units of mg/mL)*

With the assumption that the modified data represents the structure of the phantom in reality, and the HU to material conversion used by TOPAS will (for the purposes of dose) appropriately assign materials. With this sample geometry, the simulation was run using the base protocol described near the end of section 3.4.3. Figure 3.16 shows the result of the simulation plotted on MATLAB.

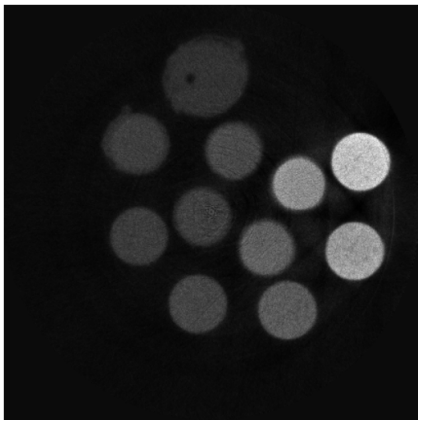

Figure 3.15: *Tomographic slice image of the material calibration phantom.*

There is high noise in this distribution of dose for many reasons. Most obviously would be the number of histories, which given the number of voxels in the scorer may not be sufficient to accurately estimate voxel dose at this resolution. Also, the HU to material conversion may not truly reflect X-ray attenuation across the entire spectrum. A MARS scan is based around acquiring data in multiple narrow energy bins, whereas conventional CT produce data representing integration of a broad energy range. Because the HU to material conversion algorithm is based off conventional CT image standards, it is possible that this negatively impacts material assignment. Of course, the strength of any such HU to material conversion is also dependent on the image quality, and some of the artefacts seen in the reconstruction image (figure 3.15) shows ring and beam hardening artefacts. The image of 'energy deposited' on the other hand shows very little noise, and that is due to the absence of mass considerations in the dose calculation. For small mass materials like air, even small levels of error can drastically change the estimated dose.

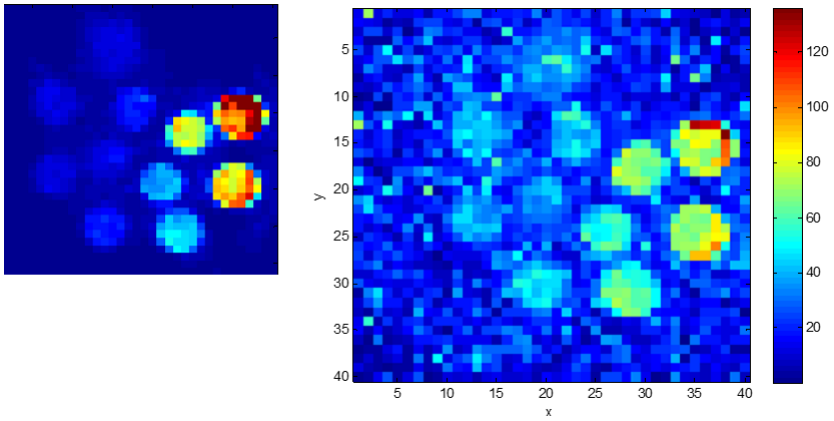

Figure 3.16: *MATLAB plots of radiation within the material calibration phantom as simulation by TOPAS with 83.2 million histories. Left- relative energy deposition. Right - plot of dose (mGy)*

Mouse scan data

For the mouse scan, a compromise had to be made because reconstruction data using the entire spectrum was not present. The energy channel chosen here was 49-82 keV, as it contained the greatest portion of the source spectrum of all the available energy bins. For the conversion from linear attenuation to HU, the reference value for μ_{water} was obtained from an accompanying material calibration phantom scan.

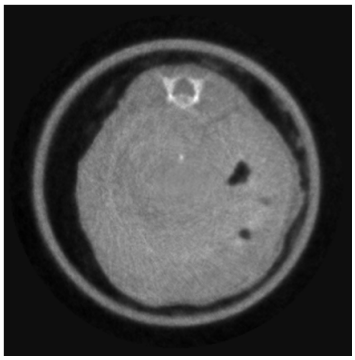

Figure 3.17: *Selected tomographic slice view of a mouse scan.*

Like the tomographic slice image, the energy deposit image in figure 3.18 shows high intensity at the dense bone region (the spine). Unlike the slice image, the energy deposit and dose images show lower intensity in the centre of the mouse and higher intensity at the edges. Similarly this effect can be observed in the phantom simulation (figure 3.16). This confirms that while highly attenuating matter absorbs more radiation energy, radiation intensity and hence dose lessens with penetration depth.

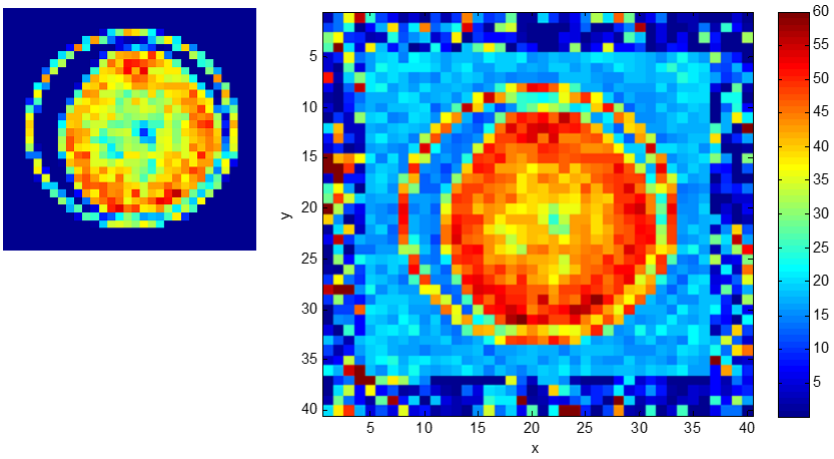

Figure 3.18: *MATLAB plot of radiation in a slice (1cm thick) as simulated by TOPAS with 83.2 million histories. Left - relative energy deposition. Right- plot of dose (mGy)*

3.6 Review

To summarise the key points of this chapter:

- A Monte Carlo simulation of pre-clinical MARS scanner was implemented with TOPAS
- The generated source beam profile was compared with literature and another Monte Carlo code. Differences in count distribution were observed, especially at higher energies.
- Preliminary simulations of dose were compared with three alternative calculation methods (simple test, kerma and fluence method, and ray-line method), demonstrating an agreement in the order of magnitude of dose estimates.
- The ray-line calculation methods served as an exploration of how a future on-board dosimetry algorithm could function. It was shown that given the assumptions made, the estimates of dose do not match Monte Carlo simulation.
- The capability of incorporating DICOM format images from MARS scans as TOPAS simulation objects was demonstrated. In addition, the ability to score dose spatially was also demonstrated.

The purpose of including Monte Carlo simulation as a tool in dosimetry is the ability to accurately estimate dose in non-trivial geometric conditions. The work in this chapter has shown the immense potential of using the Monte Carlo platform TOPAS for characterising radiation dose in MARS imaging, already showing estimates within a reasonable vicinity. Thus the groundwork has been laid for the development of a means to retrospectively determine the dose to each organ in a patient scanned by future human MARS scanners. This in turn provides a baseline for a future on-board dosimetry system.

From here, more specific verification is needed in order to establish confidence in the accuracy of simulated dose estimates. The results also raise questions regarding the true source beam profile, as differences between simulated spectra and reality would carry on into estimates of dose. Questions also remain on whether the simplifications of the inherent filtration and electron source are valid. This however, remains a task for future studies.

Chapter 4

Experimental validation measurements

4.1 Overview

The previous chapter explored how the Monte Carlo code TOPAS could be used for estimating dose in a MARS scan. However, experimental verification is necessary to have confidence in the results from TOPAS. Without proof of agreement between simulation and experiment in even simple scenarios, more complex dose distributions in CT data based material volumes have little credibility.

This chapter will describe dosimetry experiments using an ion chamber, TLD, and electronic personal dosimeters (EPD). Results from these experiments were compared with Monte Carlo simulation using TOPAS in order to determine the efficacy of the simulation. As methodologies for measuring dose in the MARS scanner with an ion chamber and TLDs have previously been explored by Ganet (described in chapter 2), they were largely adopted for these set of experiments. Rather than repeat descriptions of previously explained procedures, this chapter will focus on the modifications made to Ganet's methods and new experimental work conducted.

4.2 Measurements of CTDI with an ion chamber

The Unfors Raysafe Xi CT detector is a simple, precise, and easy to use piece of equipment that provides instant readings. It is also the primary tool used in CT quality assurance at Christchurch hospital. Hence it was ideal as a tool in verification of the Monte Carlo simulations. Because this is the second study in using the Unfors ion chamber in a MARS scanner, there is an opportunity to review and improve methodology established by Ganet for measuring dose in the MARS scanner.

4.2.1 Experimental procedures

While largely inspired by Ganet's study, for various reasons the procedure followed in this experiment incorporated a number of changes. Firstly the scan protocol was modified. This change was intended to accommodate a specific version of the MARS scanner anticipated in the near future, featuring a 3 detector camera instead of the current 1 detector camera. Ganet's study assumed a much wider detector array and hence used source-object-detector distances resulting in overly large magnification. Remaining parameters were chosen to achieve a camera response which balances signal and saturation. Thus the base protocol described earlier was adopted:

- 40 μA
- 118 kVp
- 200 mm SOD
- 48 mm ODD
- 360 projections/rotation
- 130 ms exposure time
- 25-30 ms readout time
- 1.2 (+1.8 inherent) mm Al filtration

Secondly, the phantom and holder were redesigned to take advantage of the sample bed cable system, shown in figure 4.1 C. The ion chamber equipment has

two parts (figure 2.3): first is the detector part which is inserted into the phantom and placed in the scanner. The second part is a readout unit, or electrometer, which provides power and displays the measured values; this part ideally remains outside the scanner.

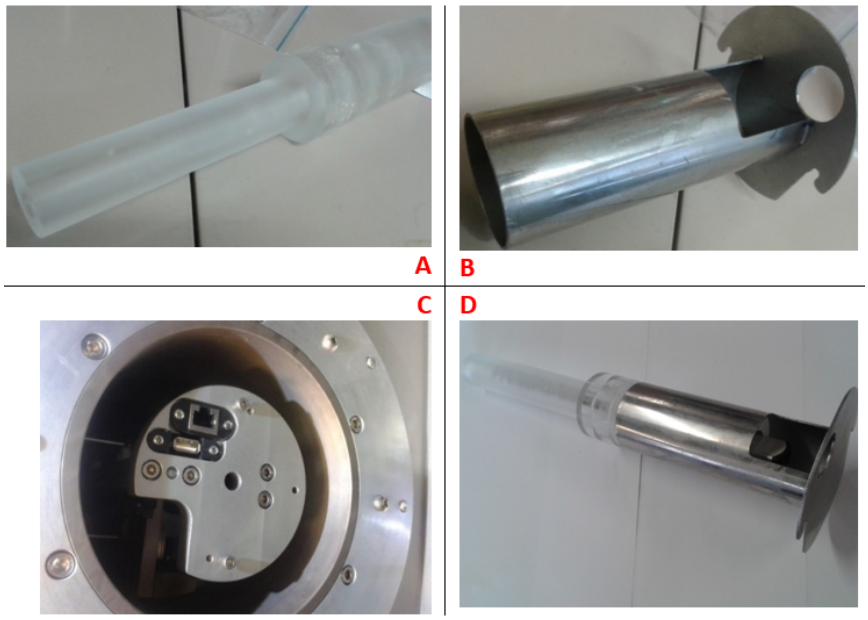

Figure 4.1: *A) Newly fabricated PMMA cylindrical phantom. B) Modified phantom holder. C) Sample bed of MARS scanner featuring cable slots. D) Combination of phantom and holder*

Previously, the cable connecting the detector unit needed to be threaded through gaps in the gantry to reach the electrometer unit. With the installation of the new sample bed featuring cable slots, it was determined that dosimetry procedures should synergize with the scanner hardware. Despite the new phantom and holder setup, the dosimetry functionality of the phantom remains the same but the extension of the phantom into the interior of the holder allows for more stable support of the pencil chamber unit. The holes added to the holder then allow manipulation of the cable coming from the chamber which can be plugged into the USB slot in the sample bed, leading to another slot on the exterior of the scanner.

The Raysafe Unfors Xi CT detector uses USB type-B mini to connect the detector unit to the electrometer unit, and so type-B mini to type-A adapters were

incorporated - one within the scanner and one at the exterior. However, it was found that USB type B-mini has 5 pins while type A only has 4. The adapters were found to ignore the signal from one of the pins, and hence the dosimeter did not operate when connected using the integrated cabling system. While this is an issue that will need to be resolved in the future, the temporary solution was the installation of the default USB type B-mini cable within the sample bed.

As a long term goal for the overarching project, scan dose must be balanced with required image quality. Scan parameters that typically affect both the dose and image quality include:

- X-ray tube voltage,
- tube current,
- source to object distance,
- added filtration.

Thus for the third modification, the experiment was expanded so that more than one value of scan dose is sought. In addition, the CTDI was measured for a series of scans with incremental variation to key parameters. This way, the accuracy of the Monte Carlo simulation in estimating dose can be gauged not only for a single set of scan parameters, but also for changes in these parameters. Should there be a mismatch between simulation and measurement, the trends in dose could also provide clues as to where the source of the mismatch comes from.

To obtain the desired data, a total of 17 scans were done; the parameters of each are listed in table 4.1. All scans were modeled off the 'base' settings described earlier, where only one parameter of interest is varied at a time. The exception to this are the scans in the 'total filtration' series, as it was found that high levels of filtration ran the risk of causing the dose rate to drop below the pencil detector's lower limit threshold of detectability; for these scans the tube current was boosted to 55 μA. Additional filtration was added by incrementally attaching small plates of Aluminium to the front of the X-ray source unit. Also note that the 'base' settings appear within multiple scan series and did not require repeating for each series.

As with Ganet's study, Gafchromic film was used to measure the field size at the position of the sample. This was found to be **15 mm**, providing the

Scan series	*kVp*	*μA*	*Total filtration*	*SOD (mm)*	*ODD (mm)*	*exposure (ms)*	*projections*
Voltage	80	40	3 mm Al	200	48	130	360
	90	40	3 mm Al	200	48	130	360
	100	40	3 mm Al	200	48	130	360
	110	40	3 mm Al	200	48	130	360
(base)	118	40	3 mm Al	200	48	130	360
Current	118	30	3 mm Al	200	48	130	360
	118	35	3 mm Al	200	48	130	360
(base)	118	40	3 mm Al	200	48	130	360
	118	45	3 mm Al	200	48	130	360
(*)	118	55	3 mm Al	200	48	130	360
Filtration	118	55	1.8 mm Al	200	48	130	360
(*)	118	55	3 mm Al	200	48	130	360
	118	55	4.2 mm Al	200	48	130	360
	118	55	4.8 mm Al	200	48	130	360
	118	55	5.4 mm Al	200	48	130	360
Distance	118	40	3 mm Al	185	48	130	360
	118	40	3 mm Al	190	48	130	360
	118	40	3 mm Al	195	48	130	360
(base)	118	40	3 mm Al	200	48	130	360
	118	40	3 mm Al	205	48	130	360

Table 4.1: *List of scans required and the parameters for each. The 'base' protocol is duplicated in each of the voltage, current, and distance scans but was not conducted multiple times in reality. The asterisks mark another duplicate set.*

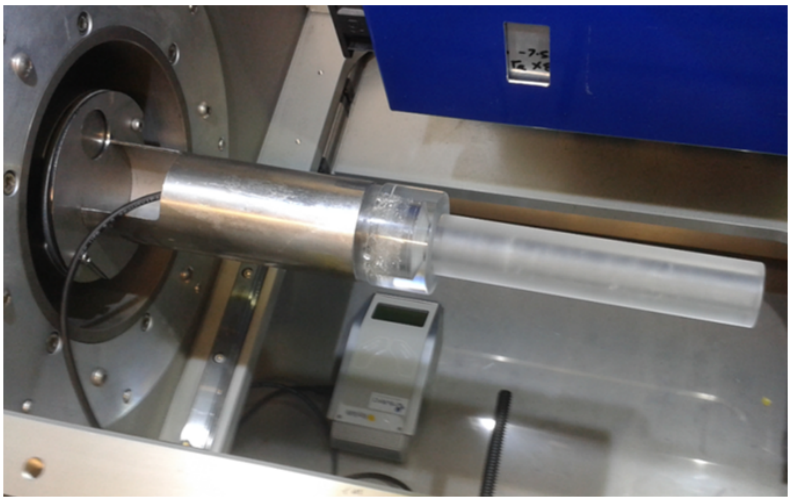

Figure 4.2: *Photograph of new pencil chamber phantom setup mounted to the sample bed. Note that this was prior to the USB mini B cable installation.*

information necessary to calculate CTDI from the raw dose measurements (see section 2.2.2).

4.2.2 Setting up equivalent TOPAS simulation

The irradiation conditions in the MARS scanner were simulated in TOPAS, using the X-ray tube and the lead collimators based on the MARS scanner design plans (figure 3.2). The phantom-ion chamber setup was represented by a water cylinder 30 mm in diameter and 100 mm in length.

Film measurements of field size were used to determining the collimator distances in simulations. Short simulations were first run and the field size was measured using planar scorers to ensure that the exposed slice thickness matched the width measured in the real scanner with Gafchromic film.

With equivalent parameters such as distances, tube voltage and filtration implemented, the simulation was run for 83.2 million histories divided between 360 angular positions (imitation of gantry rotation). This was repeated for each change in filtration, SOD, and tube voltage listed in table 4.1 totaling 13 simulation runs. Changes in current were simply represented by direct scaling of simulation output of the base protocol.

To obtain estimates of dose from raw simulated data, again the equation 3.1 was followed (using a measured scan time of 122 seconds). This was further converted to CTDI using the equation 2.4.

4.2.3 Results

The results of the 17 scans and 13 simulations are shown as graphs (figure 4.3), CTDI as a function of each key parameter and simulation plotted alongside measured values(figure 4.3). The CTDI value estimated for the base protocol by the simulation was **23.1 mGy**, while the measurement gave **21.66±1.08 mGy**. Given the uncertainty of the measurement is assumed to represent 95% confidence, this indicates a disagreement between simulation and measurement.

In figure 4.3A, while appearing to have similar linearity and trends the simulation results appears to overestimate the measured values by a near-consistent amount. For the tube voltage plot in figure 4.3B although more simulation values are observed lying within the measurement uncertainties, measured data shows a slightly shallower gradient. Figure 4.3C shows measurement falling just short of the simulation counterparts. It is possible that the mismatch at 118 kVp and 3 mm Al filtration (seen as the right-most point in figure 4.3A) carries through to changes in distance and tube current. As for the filtration plot in figure 4.3D, there appears to be slight mismatch between simulation and measurement at higher levels of filtration.

A key observation is that the addition of further layers of Aluminium decrease the dose faster than expected. One of the differences between simulation and measurement is the simulation assumes all parts of filtration can be represented by one solid block of Aluminium. In reality, the inherent filtration is distinctly separate from added filtration and even the added filtration is not made of a single block. This could provide different scattering conditions for the photons, affecting the final dose deposition.

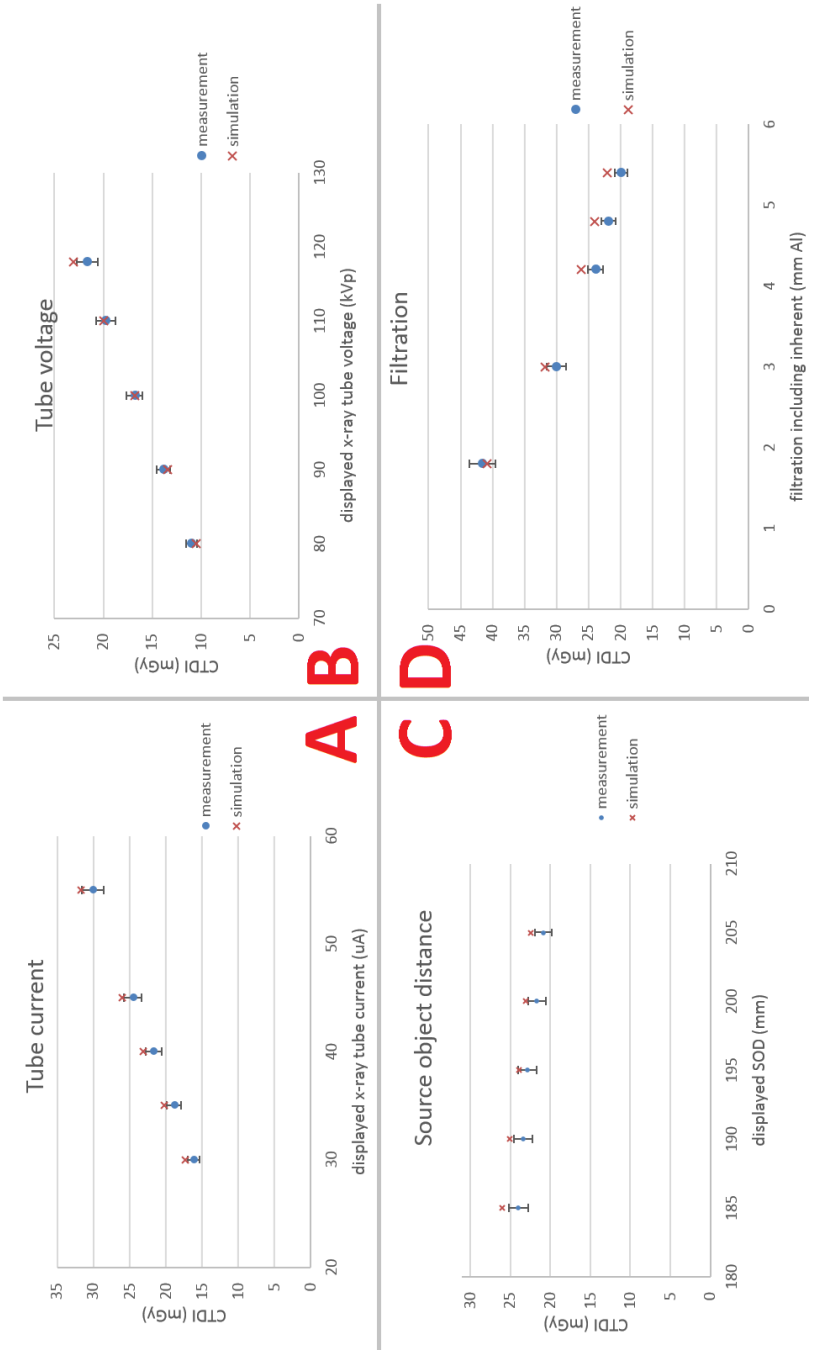

Figure 4.3: *Plot of CTDI as a function of a key X-ray tube parameter, compared between ion chamber measurement and TOPAS simulation. A) Tube current. B) Tube voltage. C) SOD. D) Filtration.*

Another thing to note was that in the simulation, no changes were made to the collimation settings at each of the different SOD values. In reality, a change in the SOD may cause the automatic collimation - a feature of the MARS scanner - to compensate. However, the expected changes in collimation were difficult to quantify physically using film and also virtually through Monte Carlo due to the penumbra. This could explain why there is a slightly greater mismatch at values of SOD further from the base value of 200 mm, as normally the collimators would open slightly when the source is brought closer to the object in order to maintain field size.

It is important to realize that these comparisons made the assumption that the ion chamber measurement reflects the dose deposited in the phantom as a whole. Hence the simulations scored absorbed dose to the entire thickness of the phantom. In reality the ion chamber pencil is only 7 mm in diameter, compared to the phantom's 30 mm diameter. In retrospect, if the simulated dose only considered the central 7 mm diameter of the phantom, then the resulting simulated dose would be much lower as the higher dose at extremities would be excluded. Figure 4.4 illustrates the distribution of higher energy near the peripheries. Such a difference between simulation and measurement may lie in the fact that the ion chamber was calibrated in free air. Backscatter and lateral scatter of radiation not accounted for during calibration would then increase the measured dose.

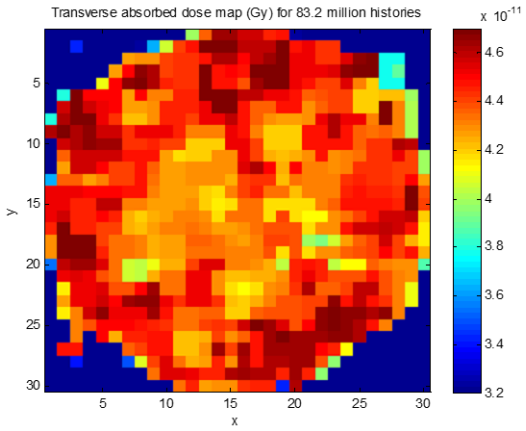

Figure 4.4: *MATLAB plot of simulated dose in water phantom viewed as a transverse cross section at the centre of the cylinder.*

4.3 TLD measurements of dose with depth

While the TLD study conducted by Ganet yielded an air kerma reading at the centre of the phantom, the attempt to characterise the air kerma profile with depth was unsuccessful. It was speculated that the the cause lay with the initial X-ray warmup phase which, while itself necessary, caused additional radiation exposure to the sample not contributing to image formation. This issue was communicated to the developers early on, and makeshift solutions were given.

The first solution was sample retraction during initial beam on: this allowed the source to turn on for warmup while the sample is kept out of the primary beam; but there is still possibility for the scattered beam to irradiate the device. As the scattered radiation is below the ion chamber's lower detectability limit, this was was considered to be an acceptable solution for the CTDI measurements. As a second solution, the gantry door is unlocked immediately after the X-ray warmup phase, allowing for a quick mounting of the sample. This option was chosen for the TLD measurements to mitigate the risk of any additional scattered X-ray exposure. The second solution was seen as less desirable for the ion chamber because of the need to handle USB cables.

With the main issue of Ganet's study considered, the following experiment aimed to re-attempt measurement of dose with depth in the phantom.

4.3.1 Experimental procedure

Equipment and calibration procedures were again used as described in section 2.3.2. For this experiment, only $phantom\ S$ from Ganet's study was used. However unlike the previous study, only a single TLD chip was inserted into the phantom at any time so as to prevent the chips from altering phantom conditions for each other during scanning. 3 TLD chips were assigned to each position within the phantom in order to gauge the extent of measurement uncertainty, resulting in a total of 15 consecutive scans of 15 individual TLD chips for a single scan protocol. The tested protocol followed the same parameters as the base protocol used for the ion chamber experiment, listed in section 4.2.1.

As with the ion chamber experiments, TOPAS simulations of equivalent conditions were conducted. The cylindrical phantom was subdivided into 5 radial bins of equal distance, representing the dose at 5 different depths. Values of scored dose were only taken from the central 10 mm (axially) of the phantom,

representing a volume that sits well within the collimated beam field.

4.4 Results

On the day of the experiment an unexpected software glitch caused the exposure and readout time per frame to vary between some scans. However, as the scan time was recorded for each scan and the dose rate was expected to behave normally, this allowed for normalisation of the measured dose to one minute. Therefore the data were still able to be used.

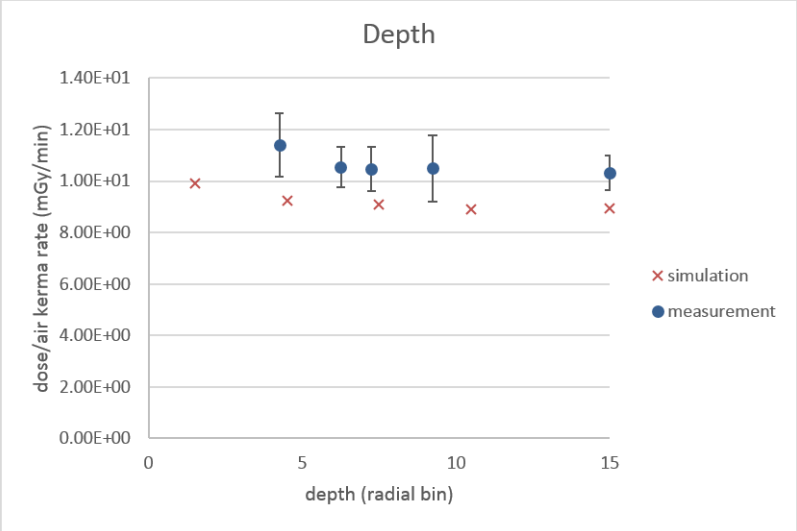

Figure 4.5: *Plot of dose or air kerma as a function of depth within phantom, compared between TLD measurement and TOPAS simulation.*

Plotted in figure 4.5 are the simulated dose rates and measured air kerma rates as a function of depth within the phantom. The values of depth for the simulation were chosen to be the distance between the phantom outer edges to the central radial point of the bin. For the measurements, the depth value was taken as the distance between the outer edge and the centre of the chip while placed inside the phantom.

As the expected scan time - as according to the ion chamber experiment - was 122 seconds, the expected scan air kerma measured at the centre of the phantom

was **20.95±0.68 mGy**. This TLD measured value agrees with the CTDI measured to be **21.66±1.08 mGy**, but is numerically lower which is expected. A TLD simply measures the dose at its location, whereas CTDI includes contribution of dose from the entire length of the ion chamber.

Kerma is only truly synonymous with absorbed dose under the condition of charged particle equilibrium. Furthermore, kerma will vary depending on the material in which it is considered. The TLD used in this experiment were calibrated for air kerma in free air, whereas the measurements were intended to assess dose to a water equivalent phantom. For the measured air kerma to be converted to absorbed dose to water, equation 4.1 was used [Podgorsak, 2005].

$$\frac{K_{col,a}}{K_{col,w}} = \frac{\Psi_a(\frac{\mu_{en}}{\rho})_a}{\Psi_w(\frac{\mu_{en}}{\rho})_w} \tag{4.1}$$

In equation 4.1, K is the kerma in material, Ψ indicates the photon fluence, $\frac{\mu_{en}}{\rho}$ is the mass energy absorption coefficient, and the subscript indicates water (w) or air (a). The conversion requires the following assumptions:

- Negligible radiative loss of energy
- Sufficient buildup is present to ensure charged particle equilibrium
- Radiation energy is sufficiently low that electron path lengths are too short for absorbed dose to exceed kerma at any point, thus $K_{col,w}$ equals absorbed dose to water
- Photo fluence does not change due to the presence of the phantom thus $\Psi_a = \Psi_w$
- The value for mass energy absorption coefficient for the polychromatic X-ray beam can be taken at a single weighted average of 54 keV: $(\frac{\mu_{en}}{\rho})_a$ = 3.57×$10^{-2} cm^2/g$ and $(\frac{\mu_{en}}{\rho})_w$ = 3.71×$10^{-2} cm^2/g$ [Hubbell and Seltzer, 2015]

With this conversion, the central TLD measurement becomes **21.77 ± 0.71 mGy** absorbed dose to water. The conversion does not significantly change the value, or bring the measurement any closer to the simulation. Unlike the ion chamber results, the simulation result is now clearly lower than measurement and even more so with the material conversion. As a comparison, **18.21 mGy**

of absorbed dose was simulated at the same position; again this is lower than the CTDI simulation as dose to the rest of the phantom is ignored here. As previously postulated, the higher measurement results may reflect the dosimeters' calibration in free air. Phantom backscatter and lateral scatter weren't accounted for in calibration, hence forming an additional portion of the measured dose.

4.5 Characterizing in-gantry dose with EPD

Electronic personal dosimeters, or EPD, refer to a class of portable electronic devices designed to be worn on the body to monitor dose or dose rate. Typically EPD are based on semiconductor technology such as silicon diodes or metal oxide field effect transistors (MOSFETs). More detailed descriptions on the general principles of operation can be found in reputed dosimetry textbooks [Attix, 2004]. It is important to note though, that many semiconductor based dosimeters exhibit a dependence on dose rate, angle, energy and temperature.

Unlike the ion chamber which required a cable, and TLD which required separate readout facilities, EPD are both completely portable and provide instant readout. For the present study they were seen as a viable tool for characterising the scattered radiation from within the MARS scanner gantry. This section details the first experiment to use EPD in characterising dose within the MARS scanner; the focus was on quantifying dose due to the primary and scattered radiation at various positions within the gantry.

4.5.1 Experimental procedure

Produced by Mirion Technologies, 6 EPD of 3 models and a USB readout device were used, as shown in figure 4.6. These were calibrated for $H_p(10)$ (measured in mSv) against water phantom to account for backscatter, but are used in this experiment essentially in free air.

These devices can be activated to store their historical radiation exposure history. The full information can be accessed by using the readout unit to extract the dose, dose rate and time. Otherwise, the dose since last activation can be directly viewed on the EPD itself.

To place an EPD in the sample position, a stiff card sheet was attached to a phantom holder, which was then clamped by the EPD. Measurements were taken

Figure 4.6: *Photograph of EPD equipment - Pairs of 3 detector models and a reader unit. A) DMC 2000S. B) DMC 2000XB. C) DMC 3000.*

at locations within the gantry marked in figure 4.7.

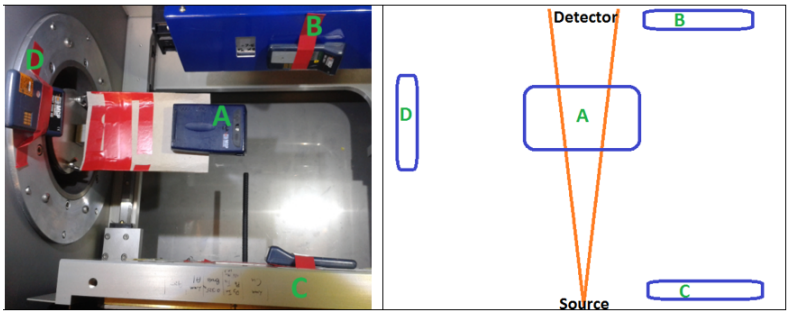

Figure 4.7: *Photograph of EPD placement within the MARS gantry, and schematic diagram of this placement relative to source beam during scanning.*

The letters correspond to the following radiation categories of interest:

(A) Primary radiation (at the sample/object position)

(B) Small angle scattered radiation (outside primary beam but near the detector)

(C) Backscatter (near the source)

(D) Lateral scatter (near the axis of gantry rotation)

As there are 4 locations and 6 separate devices, 12 scans were made such that each EPD has a reading of dose from each of the 4 positions twice. A more

robust experiment could have benefited from a larger number of repetitions, but allocated time on the MARS scanner made this difficult.

The MARS scanner again followed the base protocol used in previously described experiments, listed in section 4.2.1. However, one modification was made: the ODD was increased to 60 mm to prevent camera collision with the holder. The total scan time was measured to be 124 seconds, and for measurements at scatter locations the X-ray warm-up time of 30 seconds was included.

While energy and angular dependency of the EPD devices were considered in this study, temperature, dose and dose rate dependencies were ignored.

4.5.2 Results

Ideally, all EPD would behave consistently with each other and show the dose and dose rate at each location within the gantry. However, there were difficulties with retrieving the data from the second DMC 2000 S unit and so we have less statistical confidence in the readings given by first device. Also, values of primary beam dose at location A were significantly different between both the measurement repetitions for every individual EPD. This can be attributed to the small size and vague location of the sensitive zone within each dosimeter, which may not have been consistently placed well within the beam. Abnormally low values of dose in these instances were ignored for the following analysis.

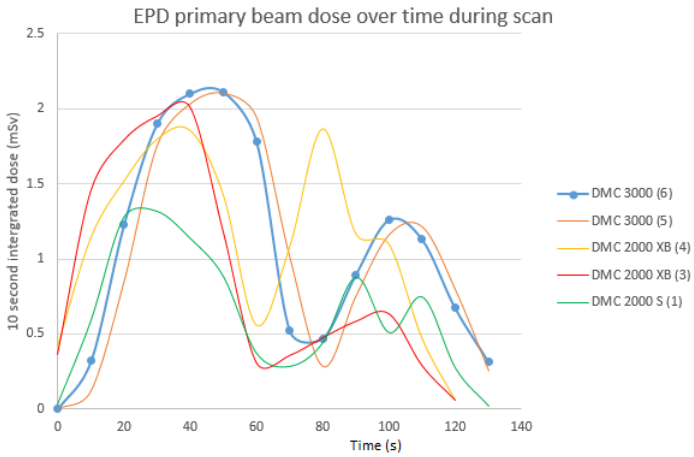

Figure 4.8: *Plot of 10s integrated dose during a scan, measured by each EPD .*

Figure 4.8 effectively shows the dose rate experienced by each EPD while at position A during a scan. There appears to be a relatively good match between the DMC 3000 units, but less so for the others. Again this could be due to inconsistent placement of the sensitive part of the dosimeters, and the different physical shape of the DMC models. Demonstrating the angular dependence, the dose exhibits two peaks during gantry rotation, being low where the X-rays pass through the narrow side of the EPD and peaking at the front-on and back-on exposures. The back-on exposures appear to give a lower peak than the front-on, possibly due to greater attenuation of one side of the EPD and more directional self-attenuation in the electronics.

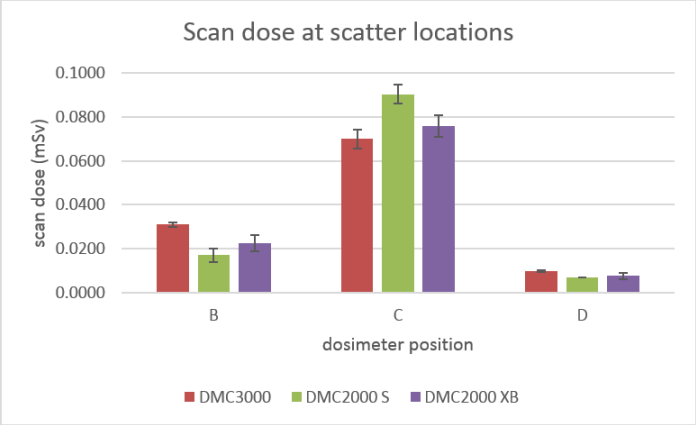

Figure 4.9: *Plot total dose measured by each EPD model at each location within the gantry during the warmup and scan period.*

Due to this angular dependence, if any comparison were to be made with other dosimeters then a factor would be needed to correct for loss of sensitivity with angle. This factor could be derived from the data in figure 4.8 by considering the area under the curve, compared to the area if the dose rate remained at peak levels throughout scanning. A continuous exposure to the peak dose rate of $\sim$2 mSv/10s (based on figure 4.8) would give a **24.8 mSv** scan dose. From [Gualdrini and Morelli, 1996], the conversion factor $H_p(10)/K_{air}$ of around 1.8 results in **13.78 mGy**.

Aside from angle, energy dependence is also an issue to be considered. Additional information provided by the manufacturer indicated that the response of the DMC3000 devices fluctuate between around 10% overestimation and 10% underestimation of the expected value over the range of photon energies. For

DMC2000S and DMC2000XB the variation was stated to be ±20%. A detailed correction for energy dependence would need to account for the spectral composition of the beam and the offset factor at every keV.

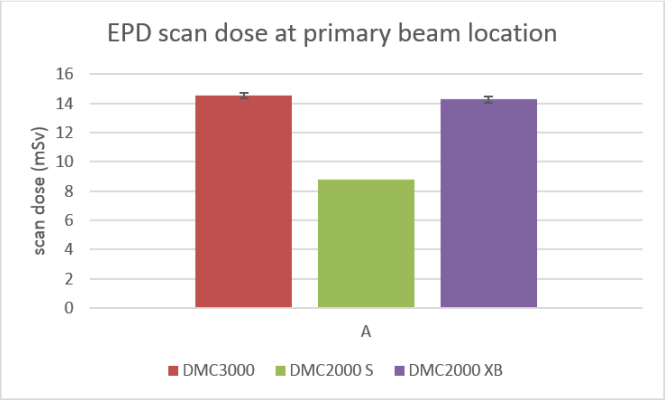

Figure 4.10: *Plot of measured dose in the primary beam for each EPD model.*

Figures 4.9 and 4.10 show the total scan dose recorded by each EPD model in each position. From this we see that there is significantly more backscatter than lateral or near-forward scatter. When comparing the two figures, it is clear that dose from scattered radiation makes up a very small portion - about 2 orders of magnitude lower than dose from the primary beam. Figure 4.10 shows the primary beam dose measured by each EPD model. DMC3000 shows good agreement with DMC2000XB, but DMC2000S appears to be significantly less sensitive.

Though the sensitivity pattern is not particularly consistent with the other positions within the gantry, a possible cause of the discrepancy is in different detection limits. The user manuals state that the DMC2000S has a detection threshold of 50 keV whereas the other two models have a threshold of 15 and 20 keV respectively. In addition, the differences seen may also relate to the low number of samples obtained, and perhaps the lack of precision in the placement of devices within the scanner.

Comparing EPD measurements with other dosimetry approaches:

1. Pencil ion chamber gave a CTDI of **21.66±1.08 mGy** (air kerma).
2. Thermoluminescent dosimeters gave **20.95±0.68 mGy** (air kerma).

3. TOPAS Monte Carlo simulation gave a CTDI of **23.1 mGy**, for entire phantom thickness. In-slice dose at central 6 mm diameter core of the phantom was scored to be **18.21 mGy** (absorbed dose to water).

4. Based on the EPD measurements, the scan dose was estimated to be **24.8 mSv** ($H_p(10)$) or **13.78 mGy** (K_{air}).

All earlier dosimetry methods point to a scan dose for the base protocol in the order of 20 mGy, but after conversion the EPD measurement appears to underestimate this. Such comparisons are made cautiously however, due to the subtle differences in measurement quantities:

- The EPD experiments did not feature a phantom, hence attenuation and scattering conditions were different. Unlike TLD and the ion chamber, the EPD were calibrated to take backscatter into account, and hence the absence of a backscattering surface during measurements means the readings are likely to under-report the dose.
- Due to the angular dependency and the course time resolution of the EPD, estimates of dose rate and hence scan dose was unreliable.
- EPD are energy dependent, and as stated before the readings could drift from baseline by up to 20% depending on energy. This would also affect the choice of $H_p(10)/K_{air}$ conversion factor, as these are derived in literature from monoenergetic sources.
- Due to the lower detectability limit of the EPD, a significant portion of the dose may be ignored.

With these factors taken into consideration, one would expect the true scan dose to be significantly higher than what the EPD have shown.

Any future studies of dose within the MARS gantry using EPD would require more precise and repeatable dosimeter placement, and a greater number of samples. Consideration for the angular dependency can be addressed by focusing on a front-on irradiation without gantry rotation. Consideration for energy dependency can be accounted for by examining the energy response data and applying corrections across the entire spectrum. Also, a physical substitute for a backscattering surface could be introduced to satisfy the devices' calibration conditions.

4.6 Review

To summarize the key points of this chapter:

- Modifications were made to Ganet's phantom and holder equipment for the ion chamber experiments. The changes provide additional stability for the ion chamber and increased compatibility of the scanner for ion chamber experiments. Cable issues still need to be addressed, however.
- Obtained dataset initially indicating general agreement between simulation and measurement across many parameter adjustments. Subtle deviations need further investigation.
- Retrospectively it was found there is reason to believe simulation of ion chamber data is overestimating dose
- TLD measurements revealed a difference with simulations at all depths. Compared with the equivalent ion chamber result however, there is little unexplainable difference.
- Evidence suggests that ion chamber and TLD calibration for air kerma in free air may be contributing to overestimations in dose when in phantom.
- EPD was shown to be a viable tool for gantry dose measurements, as long as angular and energy dependencies and device placement repeatability is addressed.
- Through use of all the dosimeters, there is consensus the scan dose is in the order of 20 mGy for parameters similar to the base protocol. This is in general agreement with Ganet's results and will be a baseline for comparison going forward.

The initial goal was to provide physical data with which to verify the Monte Carlo simulations. While data were obtained, there is evidence to suggest that the measured quantities and simulated quantities are less equivalent than first expected. With this, it is difficult to definitively say the TOPAS simulation accurately estimates dose within a few percent. Nevertheless the experiments have shown that TOPAS at the very least can approximately reproduce expected magnitudes and trends in dose with changing parameters.

Chapter 5

Conclusion

5.1 General Overview

The ultimate goal for the overarching project is the characterisation of radiation dose for the MARS system, moving towards safe and effective human scanning. Noemie Ganet initiated the project by establishing basic dosimetry procedures, quantifying scan dose to phantoms in the pre-clinical scanner. This project became a foundation for the collaboration between MARS, CERN dosimetry service, NRCS and Christchurch hospital - each of which contributed expertise or access to equipment. While the initial task was completed, issues were identified such as MARS scanner compatibility with ion chamber equipment, and the effect of hardware behaviour on TLD measurement data.

Taking Ganet's dosimetry study to the next step, the work during this thesis introduced the Monte Carlo simulation aspect and accompanying validation. Using the TOPAS code, a tool was developed which shows capability of estimating full 3D dose distribution to a range of customizable objects. In addition, there is promise that DICOM format image data from MARS scans can be imported into TOPAS for detailed retrospective dose evaluation. The validity of the DICOM import tool is an area needing further investigation. For a basic level of verification, a refined version of Ganet's methodology has shown encouraging results; all dosimetry techniques used in this thesis point to a MARS scan dose on the order of 20 mGy.

Endeavors were made to address the issues identified in Ganet's study, such as the modification of the scanner sequence to prevent exposure during warm up. A new phantom, holder, and cable setup was also designed and installed for the

ion chamber experiments. The dosimetry experiments conducted gave measurements of air kerma for a wide range of parameters; these demonstrated modest agreement with the Monte Carlo simulation tool, showing differences between 6 and 10%. It was noted that simulation and measurement mismatch partly lies in the inherent differences in measured quantities, which need to be accounted for in the future. Specifically, they may derive from the calibration conditions of the dosimeters - none of which truly enables measurement of absorbed dose within a phantom.

Continuation of the project in the future would need to re-examine the conditions set within Monte Carlo as well as those surrounding the dosimeters. Corrections or modifications are needed to account for the subtle differences between simulated and measured quantities. The path to improving agreement between simulation and measurement may involve further investigation into the X-ray source model, which demonstrated differences compared to simulations of the same source produced by other members of the MARS team. The difference in counts was shown to mainly manifest at the higher energies. Alongside basic verification, dose deposition in DICOM objects also requires examination. An accurate spatial dose simulation tool would then pave the way for a Medipix (or other spectral detector) based 3D dose reconstruction function within scanners - whether based on the previously described ray-line approach or not - allowing for instant personalized dosimetry. At such a stage, there will finally be a tool which can efficiently evaluate dose performance of any scan protocol - for any diagnostic application. These techniques in dosimetry would of course be scaled up to human sized spectral scanning.

5.2 Future work

Beyond the general comments on potential future steps in the overarching project, the following sections detail specific tasks envisioned.

5.2.1 X-ray source model

One issue with the current Monte Carlo simulation is the absence of reliable verification at the level of the X-ray source. This is crucial for a dose estimation tool, as any estimations of spatial dose deposition is strongly influenced by the spatial and spectral distribution of photons.

For validation, comparison with literature or with other simulations was the approach taken in this work. As seen in section 3.3 there were noticeable differences in the spectrum of the two simulations of between 15 to 30% at energies above 40 keV. This discrepancy is an area requiring further investigation.

As mentioned in section 3.3, Shamshad and Anjomrouz have attempted to use the Medipix3RX detector within the MARS scanner to directly record the spatial distribution of X-rays. The observed counts within a limited area near the beam center was lower than theoretical estimates by about 12%. Without full characterisation on how the detector responds to X-ray exposure of a range of energies, fluence, angle, and whether or not this changes with time, temperature, and other factors, the Medipix detector cannot truly reveal the beam properties. Obtaining the 'detector response function' is a project in itself - one which would benefit many of the studies conducted within the MARS group.

5.2.2 Precision improvements

The Monte Carlo simulation established in the present work has estimated a scan dose on the order of 20 mGy, and from various physical measurements there is a consensus the scan dose is indeed on the order of 20 mGy. Ultimately however, confirmation of the order of dose is not sufficient when the desired capability is accurate spatial dose profiling. The primary reason for this lack of exactness is the subtle differences between each quantity measured by each dosimeter, as well as that scored in simulations.

Discussed in previous chapters, it was retrospectively noted that calibration

conditions and intended calibration quantities caused the measurements to be inherently different from each other. Further studies would need to look with more scrutiny at the inherent differences between what the experiment is measuring and what the simulation is scoring. Though differences between air kerma and absorbed dose were considered for TLD measurements, and differences between personal dose equivalent and air kerma were considered for EPD measurements, these are only a part of the corrections truly required. For more completeness, the scatter contribution to the measured dose needs to be determined. Backscatter and lateral scatter due to the phantom may form a significant portion of the measured signal not accounted for during calibration, and of course the lack of a phantom or backscattering surface for the EPD measurements is also a reason for mismatch.

Hand in hand with experimental considerations, the parameter files written for TOPAS could also be further tested to accurately reflect dosimeter conditions. The simulation should address the fact that dosimeters only measure dose to their sensitive volumes, and not the phantom as a whole.

5.2.3 Verification of spatial dose in a complex object

Initial trials at importing DICOM objects into TOPAS were conducted, and they were then used to generate preliminary spatial dose maps. Similar to the dose verification of simple phantoms shown in the present work, verification of simulated dose in complex objects is also needed.

Speculation has been made in possible courses of action to address this need. One possible experiment would involve calibrating a set of TLD for absorbed dose to water in water, and inserting them at various points within the body of a mouse. A scan of the mouse would produce both image data for importing into TOPAS, and physical data on dose within the mouse.

In addition to TLD, other options for physical measurement of dose in a complex sample include OSL (optically stimulated luminescence) dosimetry and fiber optic dosimetry. Expertise in these areas has been identified in a research group based at Victoria University of Wellington, and a potential collaboration can be sought here.

5.2.4 HU to material conversion in TOPAS

The HU to material conversion used by TOPAS is a good starting tool in retrospective 3D dose mapping, but it is by no means perfect. Preliminary DICOM dose scoring has yielded promising results, although verification is still needed as stated in the previous section. Furthermore, section 3.5.2 has described a lack of consistency between the MARS DICOM output and the DICOM accepted by TOPAS; compatibility needed to be manually enforced.

The cause for concern is that the assignment of materials to DICOM objects by the simulation, and hence dose estimation in such objects may not be accurate. It entirely dependent on the HU and in turn the HU is dependent on the way the scan is performed. Assigning materials based purely on HU is a crude approach that ignores a material's different attenuations at different photon energies across the spectrum. It also does not take advantage of the material discriminating capabilities MARS imaging offers, which would otherwise provide information about the location of each material directly.

In future studies, the Hounsfield unit to material conversion function in TOPAS could be customised for material conversion which more closely matches what the MARS Material Decomposition (MD) system gives. Effort here could involve developing a new HU to material conversion option in TOPAS that interprets the post-MD dataset. A program could be made that converts a multi-channel material DICOM dataset produced by the MARS imaging chain into a single channel material coded DICOM intermediary dataset more compatible with TOPAS import.

5.2.5 Towards on-board dosimetry

Current conventions in dosimetry involve using weighing factors based on standardised human body types [ICRP103, 2007]. These conventions have seen some modification throughout history, and ultimately they hide the details of dose deposition behind a generalised value of effective dose. Conversely, knowing the *absorbed dose* to the body with high spatial precision presents a 'pure' approach to profiling patient radiation dose; and indeed this could be considered personalised dosimetry.

In the case where an illuminating X-ray beam is well known, the physical structure and composition of the irradiated object is well known, and the X-ray

beam after passing through the object is well known, there is in principle enough information to determine the pattern of radiation dose deposition. In theory, the Medipix detector fulfills the first and last of these while material decomposition promises the second. Such is the basis of a potential future on-board dosimetry system.

In practice however, the current Medipix detector demonstrates a degree of distortion which has yet to be fully characterized. This is partly described in section 5.2.1. Consequently this carries through the imaging chain and influences the quality of MD. Future work may involve investigating the detector response function - ensuring the true spectral and spatial distribution of X-rays can be inferred from detected signals. Furthermore, work will be needed in formulating an algorithm capable of deciphering the spatial dose deposition from the available data. Such a process could be based on ray-line attenuation as explored in section 3.4.3. However, this approach does not account for scattering and hence Monte Carlo simulation may be needed in determining the discrepancy introduced by scatter.

In a future where the clinical applications and diagnostic criteria of spectral CT scans are more well established, the dosimetry tools will be in place for creation of MARS specific radiation safety guidelines.

5.3 Closing

The work completed in this thesis has, continuing on from work started by Noemie Ganet, taken steps towards the bigger goal of safer spectral imaging and advanced personalised dosimetry.

This work has lit the way for further dosimetry studies that will carry the torch through to the success of MARS spectral imaging.

Literature Cited

Agostinelli, S. (2003). Geant4 collaboration. *Nucl. Instrum. Meth. Phys. Res*, 506:250–303.

Agostinelli, S., Allison, J., Amako, K., Apostolakis, J., and Araujo, H. (20038). Geant4 - a simulation toolkit. *Nuclear Instruments and Methods in Physics Research*, 506(3):350–303.

Allison, J. (2006). Geant4 collaboration. *IEEE Trans. Nucl. Sci.*, 53:270–278.

Anderson, N. G. and Butler, A. P. (2014). Clinical applications of spectral molecular imaging: potential and challenges. *Contrast Media Mol. Imaging*, 9:3–12.

Anjomrouz, M. and Shamshad, M. (2015). Beam brightness model. Medipix All Resolution Systems.

Attix, H. F. (2004). *Introduction to Radiological Physics and Radiation Dosimetry*. Wiley-Vch, Weinheim.

Berger, M. J., Hubbell, J. H., Seltzer, S. M., Chang, J., Coursey, J. S., Sukumar, R., Zucker, D. S., and Olsen, K. (1998). Xcom: Photon cross sections database.

Brenner, D. J. and Hall, E. J. (2007). Computed tomography: An increasing source of radiation exposure. *The New England Journal of Medicine*, 357(22):2277–2286.

Bushberg, T. J., Leidholdt, E. M., Boone, J. M., and a Siebert, J. (2012). *The Essential Physics of Medical Imaging 3rd Ed*. Lippincott Williams&Wilkins.

Buvat, I. and Lazaro, D. (2006). Monte carlo simulations in emission tomography and gate: an overview. *Nuclear Instruments and Methods in Physics Research A*, 567:323–329.

Cambell, M., Alozy, J., Ballabriga, R., Frojdh, E., Heijne, E., and Llopart, X. (2016). Towards a new generation of pixel detector readout chips. *Journal of Instrumentation*.

Colang, J. E., Killion, J. B., and Vano, E. (2007). Patient doses from ct: A literature review," radiologic tehnology. *Radiologic Technology*, 79.

Dance, D. R., christofides, S., Maidment, A. D., McLean, I. D., and Ng, K. H. (2014). *Diagnostic Radiology Physics: A handbook for teachers and students*. International Atomic Energy Agency, Vienna.

Dieterich, S., Ford, E., Pavord, D., and Zeng, J. (2016). *Practical Radiation Oncology Physics*. Elsevier, Phildelphia.

Ganet, N. (2014). Dosimetry studies for spectral molecular imaging of small animals with the mars ct system. Master's thesis, University of Canterbury. Phelma.

Goske, M. J., Applegate, K. E., Boylan, J., Butler, P. F., and Callahan, M. J. (2008). The imaging gently campaign: Working together to change practice. *AJR*, (190):273.

Gualdrini, G. F. and Morelli, B. (1996). Air kerma to personal dose equivalent conversion factors for the icru and iso recommended slab phantoms for photons from 20 kev to 1 mev. Technical report, Ente Per Le Nuove Technologie L'energia E L'ambeiente.

Hall, E. J. and Giaccia, A. J. (2012). *Radiobiology for the radiobiologist*. Lippincott Williams&Wilkins, Philadelphia.

Hendee, W. R. and Ritenour, E. R. (2002). *Medical Imaging Physics 4th Ed*. Wiley-Liss, New York.

Hubbell, J. H. and Seltzer, S. M. (2015). Tables of x-ray mass attenuation coefficients and mass energy-absorption coefficients from 1 kev to 20 mev for elements z = 1 to 92 and 48 additional substances of dosimetric interest.

ICRP103 (2007). Icrp publication 103: 2007 recommendations of the icrp. Technical report, International Commission on Radiological Protection.

ICRP74 (1996). Icrp publication 74: Conversion coefficients for use in radiological protection against external radiation. Technical report, International Commission on Radiological Protection.

Kalos, M. H. and Whitlock, P. A. (2008). *Monte Carlo Methods 2nd Ed*. WILEY-VCH Verlag GmbH & Co, Weinheim.

Kawrakow, I. and Rogers, D. W. (2003). The egsnrc code system: Monte carlo simulation of electron and photon transport. *Nucl. Instrum. Meth. Phys. Res*, 506:250–303.

Knoll, G. F. (2000). *Radiation detection & measurement 3rd Ed*. John Wiley and Sons, New York.

Manez, R. (2012). *Model SB-120-350 (Doc. M-SB120350, Rev 3) Installation/Operation Manual*. Source-Ray Inc.

Mattsson, S. and Soderberg, M. (2013). Dose quantities and units for radiation protection. In *Radiation Protection in Nuclear Medicine*. Springer, Berlin.

Perl, J., Shin, J., Schumann, J., Faddegon, B., and Paganetti, H. (2012). Topas: An innovative proton monte carlo platform for research and clinical applications. *Med Phys*, 39(11):6818–6837.

Podgorsak, E. B. (2005). *Radiation oncology Physics: A handbook for teachers and students*. International Atomic Energy Agency, Vienna.

Poludniowski, G. G. and Evans, P. M. (2007). Calculation of x-ray spectra emerging from an x-ray tube. part i. electron penetration characteristics in x-ray targets. *Med Phys*, 34(6):2164–2174.

Schneider, W., Bortfeld, T. B., and Schlegel, W. (2000). Correlation of ct numbers and tissue parameters needed for monte carlo simulations of clinical dose distributions. *Phys Med Biol*, 45:459–478.

Smith-Bindman, R. (2010). Is computed tomography safe? *N Engl J Med*, 363(1):1–4.

Tsapaki, V., Aldrich, J. E., and Sharma, R. (2006). Dose reduction in ct while maintaining diagnostic confidence: Diagnostic reference levels at routine head, chest, and abdominal ct-iaea coordinated research project. *Radiology*, 240:828–834.

Yu, H., Xu, Q., He, P., Bennett, J., and Aamir, R. (2012). Medipix-based spectral micro-ct. *NIH Public Access*, 21(4):583.